An efficient model for the dynamic vehicle-track-bridge-soil interaction system

Paul König, Patrick Salcher, Christoph Adam *

Unit of Applied Mechanics, University of Innsbruck, Technikerstr. 13, Innsbruck, Austria

ARTICLE INFO

ABSTRACT

A semi-analytical approach based on a lumped parameter model is presented for the analysis of the dynamic interaction system of train, track, bridge, and subsoil. Herein, the bridge and the track are modeled as Euler–Bernoulli beams, which are connected through the viscoelastic track bed. The viscoelastic supports of the bridge model capture the flexibility and damping of the subsoil below the foundations. Complex modal expansion of the deformation approximates the response of the non-classically damped bridge-soil subsystem, while a *Rayleigh–Ritz* approximation is used to efficiently describe the track deflection. To achieve the coupling of the mechanical equations of these subsystems, a variant of component mode synthesis (CMS) is applied. The mass–spring–damper (MSD) system representing the moving train is coupled to the resulting system of equations for the track-bridge-soil subsystem by a discrete substructuring technique (DST). Geometric track irregularities describing the deviation of the track from perfectly straight and smooth are accounted for by random irregularity profile functions. The results of the proposed model are compared with a finite element model to validate the modeling approach. In an application example, the effects of track irregularities and the influence of the track on the dynamic response of a bridge are discussed. The comparison of results with and without soil–structure interaction of the bridge outlines the great influence of the subsoil properties on the dynamic response in case of resonance.

1. Introduction

In recent years, the steady expansion of railway networks for high-speed traffic around the world has led to increased interest in predicting the dynamic behavior of railway bridges. However, the first investigations into the dynamic behavior of railway bridges were already carried out in 1849 by Willis and Stokes [1,2], in response to the collapse of the Chester Railway Bridge. Since at so-called resonant speeds the periodic excitation due to the constant axle spacing, track irregularities, or wheel hunting movements leads to significant amplification of displacements and accelerations, the consideration of these phenomena is of great importance for the design and assessment of railway bridges. While this dynamic amplification usually does not lead to a loss of load-bearing capacity of modern railway bridges, it increases fatigue damage over time and excessive accelerations can lead to ballast instability. This decrease in ballast stability leads to changes of the track positions and possible derailments, which must be prevented by shortening track maintenance intervals. A comprehensive review of early contributions to dynamic response prediction of railway bridges can be found in the books by Frýba [3,4]. These early works deal with the discretization of the train subsystem as moving single loads, which correspond to the axle loads of the train, and simple representations of moving mass–spring–damper (MSD) systems. In the herein used classical modal analysis, damping is usually assumed as negligible or proportional to the mass and/or stiffness of the bridge. Therefore, the solution of these systems is limited to classical damping. However, if one takes into account the damping due to wave propagation in the subsoil, modeled for example by discrete dashpots at the bridge bearings, a complex modal expansion is required to solve the moving load problem. Contributions dealing with this problem include [5–7], all of which are based on the fundamental work of Foss [8] on decoupling the equations of motion of non-proportionally damped lumped parameter systems. In the contribution of [9] and [10], an envelope impact formula is developed for a single-span bridge on elastic supports subjected to a series of moving loads and effects of resonance and cancellation are analyzed. This solution is expanded in [11], also including discrete dashpots at the bridge bearings, accounting for radiation damping of the subsoil. In a recent paper, [12], the solution for an Euler–Bernoulli beam on viscoelastic supports subject to an MSD system of the train was presented.

These insightful but also computationally efficient models are often in competition with more detailed models where the bridge is represented by a 3D finite element (FE) model crossed by MSD systems of varying degrees of sophistication [13–15]. However, due to the high computational cost, the explicit consideration of the soil in these models is hardly possible and is therefore neglected, although its large influence on the dynamic response has already been demonstrated by numerous authors [16–21]. Recent work on the decoupling of the vehicle-bridge interaction has been published in [22,23], which takes into account the influence of the moving vehicle on the natural frequencies and damping of the bridge and allows for a computationally efficient treatment of the vehicle-bridge interaction problem.

Another aspect is geometric irregularities of the track, which are not known a priori due to their randomness and have to be dealt with by stochastic simulations [24,25] if the probability of failure is considered directly. Such analyses, however, require a large number of computations and therefore a high computational efficiency, thus only simple beam models crossed by MSD systems of the train have been treated without considering the track substructure in [25–27].

In a recent contribution by the authors of this paper, [28], the component mode synthesis (CMS) approach of [29] was combined with the non-classically damped model of the bridge [12] to account for the soil–structure interaction as well as the load-distributing effects of the dynamically interacting track. This model, based on the complex modal expansion of the individual subsystems of the track and bridge beams, was used to discuss the contributions of the different dynamic subsystems on the response prediction. In particular, the effects of soil–structure interaction were demonstrated, indicating the great potential of response predictions with a realistic representation of damping related to wave propagation in the subsoil. However, the modal expansion-based approximation of the track substructure deflection requires consideration of a large number of track modes, because of the very isolated nature of the rail deflection around axle load. While the number of track modes considered was found to have little effect on the response prediction of the bridge in the case of a perfectly straight track, the presence of track irregularities required a number of 100 track modes to accurately predict the response of the bridge for the example used in [28], making this approach computationally rather inefficient.

In the present contribution, therefore, a much more efficient approach to describing the response of the track subsystem is proposed to avoid the modal expansion of the isolated nature of the track deflection in [28]. In a simplifying *Rayleigh–Ritz* approximation of the deflection of the stand-alone track subsystem, the quasi-static deflection shape of an infinitely long beam on elastic bedding is used to describe the vertical response of the track, amplified by the presence of geometric imperfections in the form of track irregularities. This simplified representation of the track is then coupled with the non-classically damped bridge beam according to the CMS used in [29] and [28]. The subsequent coupling with the train MSD system is achieved by applying a discrete substructuring technique (DST) that couples the degrees of freedom (DOFs) of the train axles with the rail deflection. This modeling strategy significantly reduces the number of DOFs required to compute the structural response and thus improves computational efficiency, making the model well suited for extensive parametric studies as well as stochastic simulations with track irregularities.

In order to validate the proposed modeling approach, the results of this approach are compared with those of an FE model in a simple example. In addition, comparative calculations are carried out with the model of [28], which show the benefits of the proposed method and provide further insight into the dynamic effects of the track on the bridge response. Furthermore, the effects of soil–structure interaction are discussed based on a comparative study.

2. Modeling approach and equations of motion

For the analysis of the dynamic response of the considered interaction system consisting of a single-span bridge with the foundation on subsoil and the track crossed by a high-speed train with constant speed v, a planar lumped parameter model is used, which is shown in Fig. 1. The conventional train considered here as an example is composed of N_c individual vehicles. The individual vehicles are modeled as moving mass–spring–damper systems consisting of a vehicle body, two bogies, and four axles, with, in total ten DOFs per vehicle. The slender bridge and the track are both modeled as uniform beams according to the Euler–Bernoulli beam theory. However, it should be noted that any other beam model, such as the Timoshenko beam, can be used without changing the computational approach presented here. Taking into account ballast stiffness and damping, the track consists of the rails resting on viscoelastic bedding. The bridge foundation is idealized by a lumped mass at each end of the bridge, with the stiffness and damping of the underlying soil represented by viscoelastic supports [12]. This model has already been used in a recent paper by the authors [28] to analyze the response of this dynamic interaction system. However, in order to understand the novel approach of this paper, the equations of motion and associated boundary conditions are also presented below.

The complete system illustrated in Fig. 1 is divided into the subsystems of the track, the bridge and the foundation on subsoil, and the train.

2.1. Track subsystem

The infinitely long Euler–Bernoulli beam representing the rails is considered to be uniform, with constant flexural rigidity EI_r and constant mass per unit length ρA_r. It rests on a viscoelastic rail bed with stiffness coefficient k_f and damping coefficient c_f. For the present investigation, these coefficients are considered as constant values. As depicted in Fig. 1, the axial coordinate x has its origin at the left bearing of the bridge. In the present modeling approach, axle loads are applied to the track only in the section $-L_0 \leq x \leq L_b + L_0$, assuming that loads applied before and after this section do not result in a dynamic response of the bridge substructure. Therefore, the length L_0 before and after the bridge must be chosen sufficiently large, which can be ensured by defining the lower limit as [28–30],

$$L_0 \geq 2\pi \sqrt[4]{\frac{4EI_r}{k_f}} \tag{1}$$

Idealizing the track with these assumptions, the equations of motion for its deflection w_r can be expressed as follows,

$$\rho A_r \ddot{w}_r(x,t) + EI_r w_{r,xxxx}(x,t) = -q_r(x,t) + f_r(x,t) \tag{2}$$

Herein, the distributed force counteracting the deformation of the rail bed, denoted as $q_r(x,t)$, is given by

$$\begin{aligned} q_r(x,t) = &k_f\left(w_r(x,t) - w_b(x,t)\Pi(x,0,L_b)\right) \\ &+ c_f\left(\dot{w}_r(x,t) - \dot{w}_b(x,t)\Pi(x,0,L_b)\right) \end{aligned} \tag{3}$$

with $w_b(x,t)$ denoting the vertical displacement of the bridge beam of the length L_b. The section where $q_r(x,t)$ is proportional to the relative vertical displacement and velocity between rails and bridge (i.e. $0 \leq x \leq L_b$) is bounded by the window function $\Pi(x,0,L_b) = H(x) - H(x-L_b)$, which consists of the two Heaviside step functions $H(x)$ and $H(x-L_b)$, respectively.

The train-rail interaction forces applied to the track are captured with the function $f_r(x,t)$,

$$f_r(x,t) = \sum_{k=1}^{N_a} F_k(t)\delta\left(x - x_k(t)\right)\Pi(t,t_{Ak},t_{Dk}) \tag{4}$$

In this equation, $F_k(t)$ represents the interaction force of the train at the kth axle position $x_k(t) = vt - l_k - L_0$ ($k = 1, \ldots, N_a$), where $-l_k - L_0$
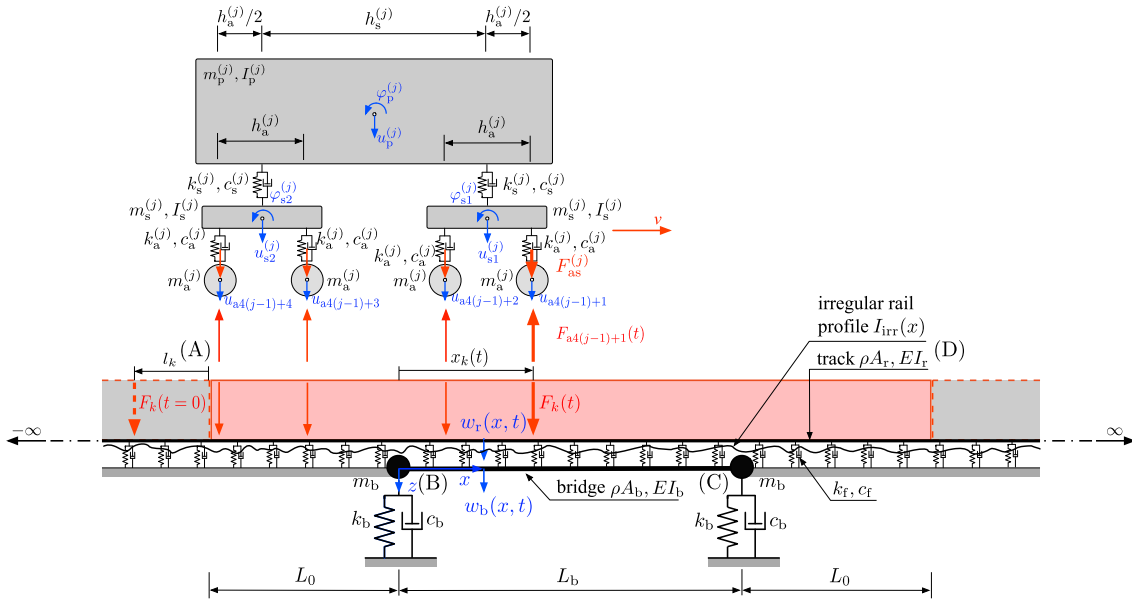
Fig. 1. Planar MSD model of the jth vehicle crossing the track resting on the bridge with viscoelastic supports.
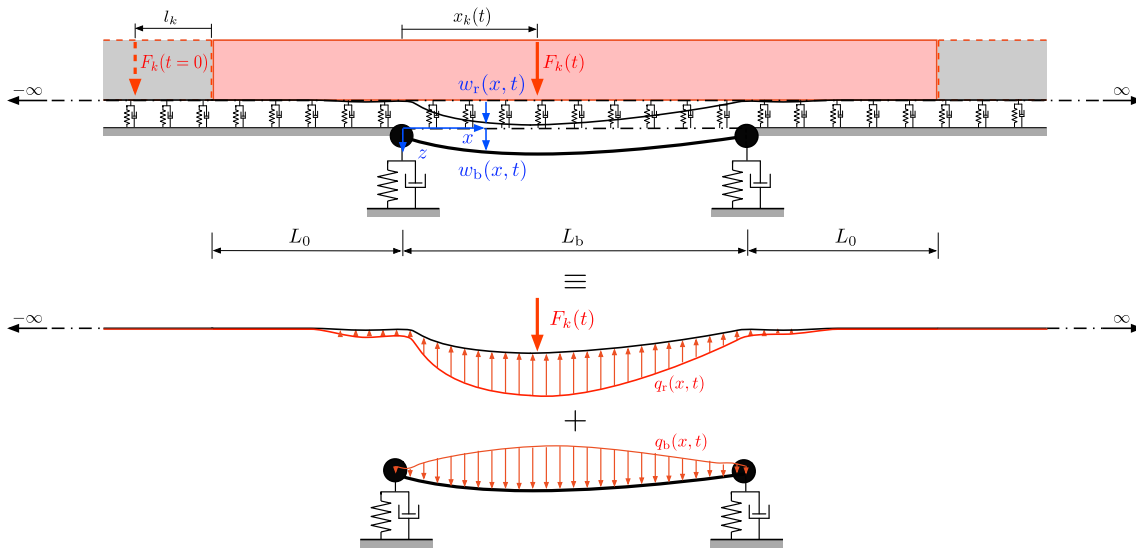*Source:* Modified from [28].

Fig. 2. Track-bridge-soil subsystem subjected to one moving interaction load and free-body diagram separating the track and the bridge-soil subsystems.
Source: Modified from [28].

is equal to the initial position of $F_k(t)$ (c.f. Figs. 1 and 2). For the conventional train model considered, the number of axles for each of the N_c vehicles is four, resulting in $N_a = 4N_c$ axles of the train. The window function $\Pi(t, t_{Ak}, t_{Dk}) = H(t - t_{Ak}) - H(t - t_{Dk})$ controls the time frame between $t_{Ak} = l_k/v$ and $t_{Dk} = (l_k + 2L_0 + L_b)/v$ in which $F_k(t)$ crosses the considered section of the track.

2.2. Bridge-soil subsystem

The bridge-soil subsystem modeled as Euler–Bernoulli beam with constant mass per unit length ρA_b and constant flexural stiffness EI_b, governed by the well-known partial differential equation in terms of the vertical displacement $w_b(x, t)$ [31]

$$\rho A_b \ddot{w}_b(x,t) + EI_b w_{b,xxxx}(x,t) = q_b(x,t) , \quad 0 \le x \le L_b \quad (5)$$

is stressed by the force

$$q_b(x,t) = k_f \left(w_r(x,t) - w_b(x,t) \right) + c_f \left(\dot{w}_r(x,t) - \dot{w}_b(x,t) \right) \quad (6)$$

transmitted through the Winkler bedding, as shown in Fig. 2.

The discrete spring–damper element at each end of the beam represents, in a simplified way, the soil below the bridge foundation [32], which is primarily excited to vibrate vertically. The spring stiffness k_b and damping parameter c_b of this element,

$$k_b = \frac{\rho_s c_w^2 A_0}{z_0} , \quad c_b = \rho_s c_w A_0 ,$$

$$z_0 = \frac{\pi}{4} (1 - \nu) \left(\frac{c_w}{c_s} \right)^2 r_0 \quad (7)$$

follow from the cone model of Wolf [33] under the assumption of a homogeneous subsoil. Here ρ_s is the density of the subsoil, A_0 represents the area of contact of the foundation, and the equivalent radius of a circular plate with the same area as the foundation is found according to $r_0 = \sqrt{A_0/\pi}$. In the expression for the shear wave velocity $c_s = \sqrt{G/\rho_s}$, G is the shear modulus of the soil. If the *Poisson*'s ratio ν of the soil is less than 1/3, then the variable c_w represents the compression

wave speed c_p, for $1/3 < \nu \leq 1/2$ the double shear wave speed c_s of the homogeneous soil [33],

$$c_\mathrm{w} = \begin{cases} c_\mathrm{p} = \sqrt{\dfrac{E_\mathrm{s}}{\rho_\mathrm{s}}} & \nu \leq 1/3 \\ 2c_\mathrm{s} = 2\sqrt{\dfrac{G}{\rho_\mathrm{s}}} & 1/3 < \nu \leq 1/2 \end{cases} \tag{8}$$

The constrained modulus E_s is related to the shear modulus G through $E_\mathrm{s} = 2G(1-\nu)/(1-2\nu)$. The stiffness coefficient k_b is a static quantity, but since the actual stiffness becomes smaller with increasing frequency, the lumped mass

$$\tilde{m}_\mathrm{g} = \frac{2.4}{\sqrt{\pi}}\left(\nu - \frac{1}{3}\right)\rho_\mathrm{s}A_0^{(3/2)} \tag{9}$$

must also be taken into account in the model for soils with a Poisson's ratio $\nu > 1/3$ [33].

The lumped mass m_b at the two ends of the bridge model is composed of the mass of the bridge foundation $\tilde{m}_1$, the mass of the soil above the foundation $\tilde{m}_2$ and the lumped soil mass $\tilde{m}_\mathrm{g}$, $m_\mathrm{b} = \tilde{m}_1 + \tilde{m}_2 + \tilde{m}_\mathrm{g}$.

Considering this lumped mass and the spring–damper elements at each end, the boundary conditions of the Euler–Bernoulli beam read as [12,28]

$$\begin{aligned}
(x=0): \quad & m_\mathrm{b}\ddot{w}_\mathrm{b}(0,t) + c_\mathrm{b}\dot{w}_\mathrm{b}(0,t) + k_\mathrm{b}w_\mathrm{b}(0,t) \\
& + EI_\mathrm{b}w_{\mathrm{b},xxx}(0,t) = 0, \\
& w_{\mathrm{b},xx}(0,t) = 0 \\
(x=L_\mathrm{b}): \quad & m_\mathrm{b}\ddot{w}_\mathrm{b}(L_\mathrm{b},t) + c_\mathrm{b}\dot{w}_\mathrm{b}(L_\mathrm{b},t) + k_\mathrm{b}w_\mathrm{b}(L_\mathrm{b},t) \\
& - EI_\mathrm{b}w_{\mathrm{b},xxx}(L_\mathrm{b},t) = 0, \\
& w_{\mathrm{b},xx}(L_\mathrm{b},t) = 0
\end{aligned} \tag{10}$$

2.3. Train subsystem

The vehicle body (subscript "p"), the two bogies (subscript "s") and the four axles with wheels (subscript "a") of the jth vehicle are represented in the model as rigid bodies with mass connected by spring–damper elements, as shown in Fig. 1. The ten DOFs of this model are composed of three rotational DOFs (rotations of the car body $\varphi_\mathrm{p}^{(j)}$ and the bogies $\varphi_\mathrm{s1}^{(j)}$ and $\varphi_\mathrm{s2}^{(j)}$) and seven translational DOFs (vertical axle displacements $u_{\mathrm{a}4(j-1)+l}$ ($l = 1, \ldots, 4$ axles of the jth vehicle); vertical displacement of the wagon body $u_\mathrm{p}^{(j)}$; vertical displacement of the bogies $u_\mathrm{s1}^{(j)}$, $u_\mathrm{s2}^{(j)}$) [34,35], are combined in the vector $\mathbf{u}_\mathrm{c}^{(j)}$,

$$\begin{aligned}
\mathbf{u}_\mathrm{c}^{(j)} = \big[& u_\mathrm{p}^{(j)}, \varphi_\mathrm{p}^{(j)}, u_\mathrm{s1}^{(j)}, \varphi_\mathrm{s1}^{(j)}, u_\mathrm{s2}^{(j)}, \varphi_\mathrm{s2}^{(j)}, u_{\mathrm{a}4(j-1)+1}, u_{\mathrm{a}4(j-1)+2}, u_{\mathrm{a}4(j-1)+3}, \\
& u_{\mathrm{a}4(j-1)+4} \big]^\mathrm{T}
\end{aligned} \tag{11}$$

Herein the index $4(j-1)+l$ relates the lth axle of the jth vehicle to the global axle number k, thus $k = 4(j-1)+l$.

Since the horizontal interaction between the N_c individual vehicles is neglected, the combined equations of motion of the entire train read [14]

$$\mathbf{M}_\mathrm{c}\ddot{\mathbf{u}}_\mathrm{c} + \mathbf{C}_\mathrm{c}\dot{\mathbf{u}}_\mathrm{c} + \mathbf{K}_\mathrm{c}\mathbf{u}_\mathrm{c} = \mathbf{F}_\mathrm{c} \tag{12}$$

where $\mathbf{M}_\mathrm{c}$, $\mathbf{C}_\mathrm{c}$ and $\mathbf{K}_\mathrm{c}$ represent the mass, damping and stiffness matrices of the train, which are composed of the system matrices of the individual vehicles,

$$\begin{aligned}
\mathbf{M}_\mathrm{c} &= \mathrm{diag}\left[\mathbf{M}_\mathrm{c}^{(1)}, \mathbf{M}_\mathrm{c}^{(2)}, \ldots, \mathbf{M}_\mathrm{c}^{(N_\mathrm{c})}\right], \quad \mathbf{C}_\mathrm{c} = \mathrm{diag}\left[\mathbf{C}_\mathrm{c}^{(1)}, \mathbf{C}_\mathrm{c}^{(2)}, \ldots, \mathbf{C}_\mathrm{c}^{(N_\mathrm{c})}\right] \\
\mathbf{K}_\mathrm{c} &= \mathrm{diag}\left[\mathbf{K}_\mathrm{c}^{(1)}, \mathbf{K}_\mathrm{c}^{(2)}, \ldots, \mathbf{K}_\mathrm{c}^{(N_\mathrm{c})}\right], \quad \mathbf{u}_\mathrm{c} = \left[\mathbf{u}_\mathrm{c}^{(1)}, \mathbf{u}_\mathrm{c}^{(2)}, \ldots, \mathbf{u}_\mathrm{c}^{(N_\mathrm{c})}\right]^\mathrm{T}
\end{aligned} \tag{13}$$

The vehicle system matrices $\mathbf{M}_\mathrm{c}^{(j)}, \mathbf{C}_\mathrm{c}^{(j)}, \mathbf{K}_\mathrm{c}^{(j)}$ are specified in [12,14]. The interaction forces between the vehicle and the track subsystems at the position of each axle of the N_c vehicles shown in Fig. 1,

$$\begin{aligned}
\mathbf{F}_\mathrm{c}^{(j)} = \big[& 0, 0, 0, 0, 0, 0, F_\mathrm{as}^{(j)} + F_{\mathrm{a}4(j-1)+1}, F_\mathrm{as}^{(j)} + F_{\mathrm{a}4(j-1)+2}, F_\mathrm{as}^{(j)} + F_{\mathrm{a}4(j-1)+3}, \\
& F_\mathrm{as}^{(j)} + F_{\mathrm{a}4(j-1)+4} \big]^\mathrm{T}
\end{aligned} \tag{14}$$

are combined in the force vector

$$\mathbf{F}_\mathrm{c} = \left[\mathbf{F}_\mathrm{c}^{(1)}, \mathbf{F}_\mathrm{c}^{(2)}, \ldots, \mathbf{F}_\mathrm{c}^{(N_\mathrm{c})}\right]^\mathrm{T} \tag{15}$$

Each interaction force consists of a dynamic component, $F_{\mathrm{a}4(j-1)+l}$ and a static component $F_\mathrm{as}^{(j)}$ from the vehicle gravity load distributed over the four axles,

$$F_\mathrm{as}^{(j)} = \frac{g}{4}\left(m_\mathrm{p}^{(j)} + 2m_\mathrm{s}^{(j)} + 4m_\mathrm{a}^{(j)}\right) \tag{16}$$

where g denotes the acceleration of gravity.

3. Approach for the analysis of the bridge-soil and the track subsystems

Based on the CMS method proposed in [28,36], in the following the bridge-soil and track subsystems are coupled. In contrast to the modal series expansion of the deformations of both subsystems proposed in [29], however, only the response of the non-classically damped bridge-soil subsystem is approximated by a modal series. The displacement of the stand-alone track, on the other hand, is described by a *Rayleigh–Ritz* approximation. The modal properties of the bridge-ground subsystem can be found in Appendix A, while in Appendix B the approximation of the track substructure is described.

3.1. Series expansion of the response variables

The modal series expansion of the vertical displacement $w_\mathrm{b}(x,t)$ of the bridge-soil subsystem into N_b complex modes results in

$$w_\mathrm{b}(x,t) \approx \sum_{m=1}^{N_\mathrm{b}} y_\mathrm{b}^{(m)}(t)\varPhi_\mathrm{b}^{(m)}(x) + \sum_{m=1}^{N_\mathrm{b}} \bar{y}_\mathrm{b}^{(m)}(t)\bar{\varPhi}_\mathrm{b}^{(m)}(x) \tag{17}$$

with $\varPhi_\mathrm{b}^{(m)}(x)$ denoting the mth complex eigenfunction and $\bar{\varPhi}_\mathrm{b}^{(m)}(x)$ its complex conjugate counterpart (see Eq. (A.1), Appendix A). The variables $y_\mathrm{b}^{(m)}$ and $\bar{y}_\mathrm{b}^{(m)}$ are the corresponding complex modal coordinate and its complex conjugate equivalent, respectively.

According to the CMS method used in [28,29], the displacement $w_\mathrm{r}(x,t)$ of the track is decomposed into two parts,

$$w_\mathrm{r}(x,t) = w_\mathrm{r}^{(\mathrm{f})}(x,t) + w_\mathrm{r}^{(\mathrm{b})}(x,t) \tag{18}$$

The variable $w_\mathrm{r}^{(\mathrm{f})}(x,t)$ represents the deflection of the stand-alone track on viscoelastic bedding (i.e. Fig. 3(a)) induced by the interaction force $f_\mathrm{r}(x,t)$, governed by the equation of motion Eq. (2) without the terms associated with the bridge displacement w_b. As a novelty and in contrast to the approach used in [28], $w_\mathrm{r}^{(\mathrm{f})}(x,t)$ is approximated in the sense of *Rayleigh–Ritz* by a sum of individual deflection shapes,

$$w_\mathrm{r}^{(\mathrm{f})}(x,t) \approx \sum_{k=1}^{N_\mathrm{a}} \varphi_\mathrm{r}(x - x_k(t))y_{\mathrm{r}k}(t) \tag{19}$$

Herein $\varphi_\mathrm{r}(x - x_k(t))$ is the kth static deflection shape of the stand-alone track on elastic bedding (see Eq. (B.1)) centered around the kth axle at the position $x_k(t)$, due to the single load $F_k(t)$. The kth deflection shape is scaled to the maximum value of one at the respective axle position $x - x_k(t) = 0$ and is moving together with the corresponding axle load $F_k(t)$ in axial direction at the constant train speed v. Each of these deflection shapes is assumed to adequately describe the deflection of the stand-alone track on viscoelastic bedding due to the corresponding axle load, thus the number of *Rayleigh–Ritz* approximations in Eq. (19) is equal to the number of axles of the train N_a. The kth deflection shape is multiplied with the time-dependent coordinate $y_{\mathrm{r}k}(t)$, to represent the deflection resulting from the kth interaction force F_k. In contrast to the detailed descriptions of the track deflection, used for example in [4,37,38] this approach allows for an efficient approximation of the response contribution $w_\mathrm{r}^{(\mathrm{f})}(x,t)$.

The second contribution in Eq. (18), $w_\mathrm{r}^{(\mathrm{b})}(x,t)$, can be thought of as the track response contribution due to the bridge displacement w_b [29],
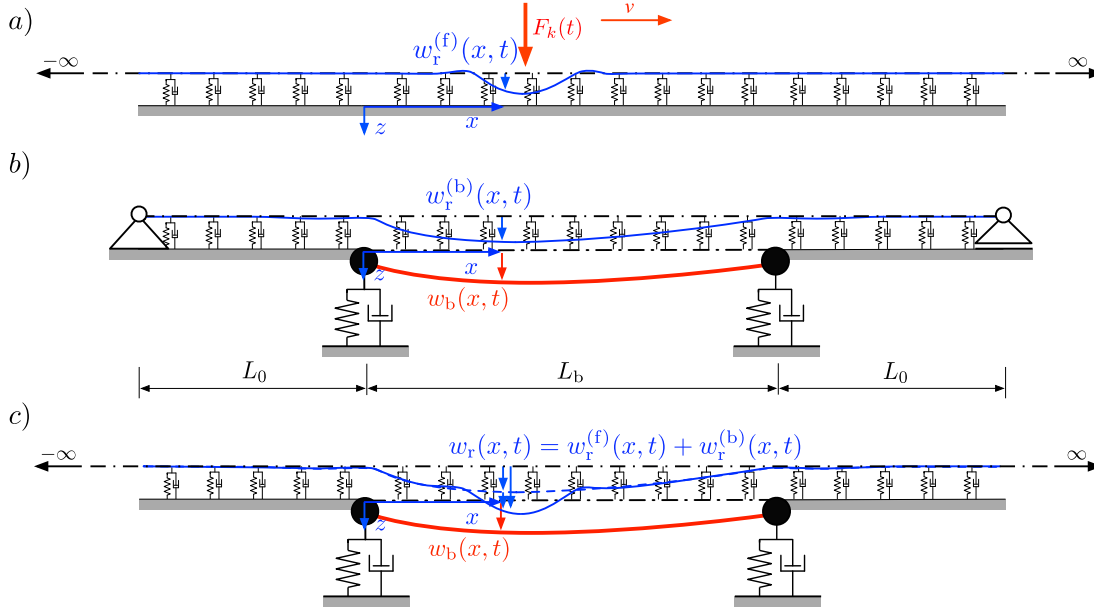
Fig. 3. Individual response contributions (a) deflection $w_r^{(f)}(x,t)$ of the track on viscoelastic bedding resulting from the interaction force $F_k(t)$, (b) deflection $w_r^{(b)}(x,t)$ resulting from the bridge deformation and (c) combined deflection of the track $w_r(x,t)$ and displacement of the bridge $w_b(x,t)$.
Source: Modified from [28].

as visualized in Fig. 3(b). According to [29], $w_r^{(b)}$ is modally expanded, involving the modal coordinates $y_b^{(m)}(t)$ and $\bar{y}_b^{(m)}(t)$ [28],

$$w_r^{(b)}(x,t) \approx \sum_{m=1}^{N_b} y_b^{(m)}(t)\Psi_r^{(m)}(x) + \sum_{m=1}^{N_b} \bar{y}_b^{(m)}(t)\bar{\Psi}_r^{(m)}(x) \tag{20}$$

where $\Psi_r^{(m)}(x)$ is an appropriately chosen shape function of the track and $\bar{\Psi}_r^{(m)}(x)$ its complex conjugate counterpart. To find a suitable set of shape functions, the mth modal contribution of the deformations $w_r^{(b)(m)}(x,t) = \Psi_r^{(m)}(x)y_b^{(m)}(t)$ and $w_b^{(m)}(x,t) = \Phi_b^{(m)}(x)y_b^{(m)}(t)$ are substituted into Eqs. (2) and (3) without the time-dependent terms, yielding the following quasi-static relation,

$$EI_r\Psi_{r,xxxx}^{(m)}(x) + k_f(x)\Psi_r^{(m)}(x) = k_f(x)\Phi_b^{(m)}(x)\Pi(x,0,L_b) \tag{21}$$

This differential equation, which relates the unknown mth shape function of the track $\Psi_r^{(m)}(x)$ to the known mth eigenfunction of the bridge $\Phi_b^{(m)}(x)$, is solved numerically for $\Psi_r^{(m)}(x)$. However, this numerical solution requires the definition of artificial boundary conditions in the track beam as shown in Fig. 3,

$$w_r^{(b)}(x = -L_0, t) = 0, \qquad w_r^{(b)}(x = L_b + L_0, t) = 0$$
$$w_{r,xx}^{(b)}(x = -L_0, t) = 0, \qquad w_{r,xx}^{(b)}(x = L_b + L_0, t) = 0 \tag{22}$$

thus limiting $w_r^{(b)}$ to the range $-L_0 \leq x \leq L_b + L_0$. Since the track deflection resulting from the displacement of the bridge approaches zero with increasing distance from the bridge, the position of these artificial boundary conditions is chosen at $x = -L_0$ and $x = L_b + L_0$, which satisfies Eq. (1). Accordingly, the complex conjugate $\bar{\Psi}_r^{(m)}$ associated with $\bar{\Phi}_b^{(m)}$ can be found.

3.2. Coupling of the soil-bridge and the track subsystem

First, the equations of motion of the soil-bridge and the track subsystem (Eq. (5) and (2)) are put into the following form,

$$
\begin{bmatrix} \rho A_b & 0 \\ 0 & \rho A_r \end{bmatrix}
\begin{bmatrix} \ddot{w}_b(x,t) \\ \ddot{w}_r(x,t) \end{bmatrix}
+
\begin{bmatrix} EI_b & 0 \\ 0 & EI_r \end{bmatrix}
\begin{bmatrix} w_{b,xxxx}(x,t) \\ w_{r,xxxx}(x,t) \end{bmatrix}
$$
$$
=
\begin{bmatrix} -k_f & k_f \\ k_f & -k_f \end{bmatrix}
\begin{bmatrix} w_b(x,t) \\ w_r(x,t) \end{bmatrix}
+
\begin{bmatrix} -c_f & c_f \\ c_f & -c_f \end{bmatrix}
\begin{bmatrix} \dot{w}_b(x,t) \\ \dot{w}_r(x,t) \end{bmatrix}
+
\begin{bmatrix} 0 \\ f_r \end{bmatrix} \tag{23}
$$

A compact notation of the series approximations of the deflections w_b and w_r according to Eqs. (17), (19) and (20) reads

$$
\begin{bmatrix} w_b(x,t) \\ w_r(x,t) \end{bmatrix}
=
\begin{bmatrix} w_b(x,t) \\ w_r^{(b)}(x,t) + w_r^{(f)}(x,t) \end{bmatrix}
= \Lambda \mathbf{h}_B \tag{24}
$$

where the matrix

$$
\Lambda =
\begin{bmatrix} \Phi_b(x)^T & \mathbf{0} \\ \Psi_r(x)^T & \Phi_r^*(x)^T \end{bmatrix} \tag{25}
$$

is made up of the vector of the complex-valued eigenfunctions of the bridge-soil subsystem, $\Phi_b(x)$, the vector of shape functions of the deflection of the stand-alone track, $\Phi_r^*(x)$, and the vector of the shape functions of the track due to the bridge displacement, $\Psi_r(x)$,

$$\Phi_b = \left[\Phi_b^{(1)}, \Phi_b^{(2)}, \ldots, \Phi_b^{(N_b)}, \bar{\Phi}_b^{(1)}, \bar{\Phi}_b^{(2)}, \ldots, \bar{\Phi}_b^{(N_b)}\right]^T,$$

$$\Psi_r = \left[\Psi_r^{(1)}, \Psi_r^{(2)}, \ldots, \Psi_r^{(N_b)}, \bar{\Psi}_r^{(1)}, \bar{\Psi}_r^{(2)}, \ldots, \bar{\Psi}_r^{(N_b)}\right]^T, \tag{26}$$

$$\Phi_r^* = \left[\varphi_r(x - x_1), \varphi_r(x - x_2), \ldots, \varphi_r(x - x_{N_a})\right]^T$$

and the vector

$$\mathbf{h}_B = \begin{bmatrix} \mathbf{y}_b(t) \\ \mathbf{y}_r(t) \end{bmatrix} \tag{27}$$

which combines the modal coordinates of the bridge-soil subsystem,

$$\mathbf{y}_b = \left[y_b^{(1)}, y_b^{(2)}, \ldots, y_b^{(N_b)}, \bar{y}_b^{(1)}, \bar{y}_b^{(2)}, \ldots, \bar{y}_b^{(N_b)}\right]^T \tag{28}$$

and the time-dependent coordinates of the track subsystem,

$$\mathbf{y}_r = \left[y_{r1}, y_{r2}, \ldots, y_{rN_a}\right]^T \tag{29}$$

Eq. (24) is then substituted into Eq. (23), this expression is premultiplied by Λ^T and integrated over the track length $-\infty \leq x \leq \infty$. This leads, taking into account the orthogonality relations of the bridge-soil subsystem (cf. Appendix A) and the *Rayleigh–Ritz* approximation of the track deflection (cf. Appendix B), to the following coupled set of equations of motion expressed by the vector of modal coordinates $\mathbf{h}$ of both subsystems,

$$\mathbf{M}_B(t)\ddot{\mathbf{h}}_B(t) + \mathbf{C}_B(t)\dot{\mathbf{h}}_B(t) + \mathbf{K}_B(t)\mathbf{h}_B(t) = \mathbf{f}_B(t) \tag{30}$$

with the system matrices $\mathbf{M}_B$, $\mathbf{C}_B$ and $\mathbf{K}_B$,

$$\mathbf{M}_B = \begin{bmatrix} \mathbf{0} & \mathbf{M}_{br} \\ \mathbf{M}_{rb} & \mathbf{M}_r \end{bmatrix}, \quad \mathbf{C}_B = \begin{bmatrix} \mathbf{A}_b + \Delta\mathbf{C}_b + \Delta\mathbf{M}_b\mathbf{S}_b & \mathbf{C}_{br} \\ \mathbf{C}_{rb} & \mathbf{C}_r \end{bmatrix},$$

$$\mathbf{K}_B = \begin{bmatrix} \mathbf{B}_b + \Delta\mathbf{K}_b & \mathbf{K}_{br} \\ \mathbf{K}_{rb} & \mathbf{K}_r \end{bmatrix} \tag{31}$$

Herein the sub-matrices $\mathbf{A}_b$ and $\mathbf{B}_b$ are diagonal matrices composed of the coefficients for the orthogonality conditions,

$$\mathbf{A}_b = \mathrm{diag}\left[a_b^{(1)}, a_b^{(2)}, \ldots, a_b^{(N_b)}, \bar{a}_b^{(1)}, \bar{a}_b^{(2)}, \ldots, \bar{a}_b^{(N_b)} \right],$$

$$\mathbf{B}_b = \mathrm{diag}\left[b_b^{(1)}, b_b^{(2)}, \ldots, b_b^{(N_b)}, \bar{b}_b^{(1)}, \bar{b}_b^{(2)}, \ldots, \bar{b}_b^{(N_b)} \right] \tag{32}$$

specified in Appendix A, and $\mathbf{S}_b$ is a diagonal matrix consisting of the complex natural frequencies of the bridge model (cf. Appendix A),

$$\mathbf{S}_b = \mathrm{diag}\left[s_b^{(1)}, s_b^{(2)}, \ldots, s_b^{(N_b)}, \bar{s}_b^{(1)}, \bar{s}_b^{(2)}, \ldots, \bar{s}_b^{(N_b)} \right] \tag{33}$$

The sub-matrices $\mathbf{M}_r$, $\mathbf{C}_r$ and $\mathbf{K}_r$ that result from the integration over the infinite track beam on viscoelastic bedding assuming a symmetric, quasi-static deflection shape (c.f. Eqs. (B.1) and (B.5)), are diagonal,

$$\mathbf{M}_r = \mathrm{diag}\left[\frac{3}{2\beta}\rho A_r, \ldots, \frac{3}{2\beta}\rho A_r \right], \quad \mathbf{C}_r = \mathrm{diag}\left[\frac{3}{2\beta}c_f, \ldots, \frac{3}{2\beta}c_f \right],$$

$$\mathbf{K}_r = \mathrm{diag}\left[\frac{2}{\beta}k_f, \ldots, \frac{2}{\beta}k_f \right] \tag{34}$$

because the non-diagonal elements are small compared to the diagonal entries and therefore assumed to be zero. The reason for this is that the static deflection around each axle load is strongly isolated for common parameter configurations of the rail bed. Furthermore, it should be noted that the N_a diagonal entries within a matrix are the same since the shape for all shape functions of the stand-alone infinite track beam is the same regardless of the position of the axle load. The time-dependent coordinates y_{rk}, $k = 1, \ldots, N_a$ cumulated in the vector $\mathbf{y}_r$, Eq. (29), of the partial response $w_r^{(f)}$ of the track are thus decoupled from each other and have the form of a single degree of freedom (SDOF) system. Each of these SDOF systems thus describes the partial response $w_r^{(f)}$ at a specific axle position. These SDOF systems are coupled to the bridge-soil subsystem by the sub-matrices denoted by the index "br" and "rb", respectively,

$$\mathbf{M}_{br}(t) = \mathbf{M}_{rb}^T(t) = \rho A_r \int_{-L_0}^{L_b+L_0} \boldsymbol{\Psi}_r \boldsymbol{\Phi}_r^{*T} dx,$$

$$\mathbf{C}_{br}(t) = \mathbf{C}_{rb}^T(t) = c_f \int_{-L_0}^{L_b+L_0} \boldsymbol{\Psi}_r \boldsymbol{\Phi}_r^{*T} dx - c_f \int_0^{L_b} \boldsymbol{\Phi}_b \boldsymbol{\Phi}_r^{*T} dx \tag{35}$$

and

$$\mathbf{K}_{br}(t) = EI_r \int_{-L_0}^{L_b+L_0} \boldsymbol{\Psi}_r \boldsymbol{\Phi}_{r,xxxx}^{*T} dx + k_f \int_{-L_0}^{L_b+L_0} \boldsymbol{\Psi}_r \boldsymbol{\Phi}_r^{*T} dx - k_f$$

$$\times \int_0^{L_b} \boldsymbol{\Phi}_b \boldsymbol{\Phi}_r^{*T} dx, \tag{36}$$

$$\mathbf{K}_{rb}(t) = \mathbf{0}$$

Herein, the limits of integration result from the range of definition of $\boldsymbol{\Psi}_r$ and $\boldsymbol{\Phi}_b$. The time dependence of these matrices results from the movement of each deformation shape of the track with the corresponding axle of the train with the speed v. Fourfold integration by parts of $\mathbf{K}_{br}$ together with the relation according to Eq. (21) and the boundary conditions according to Eq. (22) shows that $\mathbf{K}_{br}$ can be expressed by the function values of $\boldsymbol{\Psi}_r$ and $\boldsymbol{\Phi}_r^*$ and their derivatives at the limits of integration $x = -L_0$ and $x = L_b + L_0$,

$$\mathbf{K}_{br}(t) = EI_r \left(-\boldsymbol{\Psi}_{r,x}(L_b+L_0)\boldsymbol{\Phi}_{r,xx}^{*T}(L_b+L_0, t) + \boldsymbol{\Psi}_{r,x}(-L_0)\boldsymbol{\Phi}_{r,xx}^{*T}(-L_0, t) \right.$$

$$\left. -\boldsymbol{\Psi}_{r,xxx}(L_b+L_0)\boldsymbol{\Phi}_r^{*T}(L_b+L_0, t) + \boldsymbol{\Psi}_{r,xxx}(-L_0)\boldsymbol{\Phi}_r^{*T}(-L_0, t) \right) \tag{37}$$

Since the shape functions in $\boldsymbol{\Psi}_r$ and their derivatives approach zero with increasing distance from the bridge, the influence of this matrix

on the system response is very small if L_0 is reasonably long (such as defined in Eq. (1)). Hence, $\mathbf{K}_{br}(t)$ is assumed as $\mathbf{0}$.

The force vector $\mathbf{f}_B$ in Eq. (30),

$$\mathbf{f}_B = \begin{bmatrix} \mathbf{f}_b \\ \mathbf{f}_r \end{bmatrix} \tag{38}$$

is composed of the force vectors $\mathbf{f}_b$ and $\mathbf{f}_r$, which capture the effect of the vehicle interaction forces F_k ($k = 1, \ldots, N_a$) on the bridge-soil subsystem and the track subsystem, respectively, with

$$\mathbf{f}_b = \boldsymbol{\Psi}_r \boldsymbol{\Pi}\mathbf{F}, \quad \mathbf{F} = \left[F_1, F_2, \ldots, F_{N_a} \right]^T \tag{39}$$

$$\boldsymbol{\Pi} = \mathrm{diag}\left[\Pi(t, t_{A1}, t_{B1}), \Pi(t, t_{A2}, t_{D2}), \ldots, \Pi(t, t_{AN_a}, t_{DN_a}) \right] \tag{40}$$

$$\boldsymbol{\Psi}_r = \left[\boldsymbol{\Psi}_r(x_1), \boldsymbol{\Psi}_r(x_2), \ldots, \boldsymbol{\Psi}_r(x_{N_a}) \right] \tag{41}$$

and

$$\mathbf{f}_r = \boldsymbol{\Phi}_r^* \boldsymbol{\Pi}\mathbf{F} = \boldsymbol{\Pi}\mathbf{F} \tag{42}$$

Eq. (42) results from the simplifying assumption that the kth deflection shape $\varphi_r(x - x_k)$ does not lead to a deflection at the positions of the adjacent axles x_{k-1} and x_{k+1}, given their isolated shape. Therefore, the matrix $\boldsymbol{\Phi}_r^*$ in Eq. (42) reads as

$$\boldsymbol{\Phi}_r^* = \left[\boldsymbol{\Phi}_r^*(x_1), \boldsymbol{\Phi}_r^*(x_2), \ldots, \boldsymbol{\Phi}_r^*(x_{N_a}) \right] \approx \mathbf{I}_r \tag{43}$$

with $\mathbf{I}_r$ denoting an identity matrix of size $[N_a \times N_a]$.

If the effect of the train on the track-bridge-soil system is described in a simplified way by a single load model, where the interaction forces in $\mathbf{F}$ correspond to the static axle loads, Eq. (30) can be solved numerically by applying the Newmark β-time integration scheme [39]. The time-dependent matrices in Eq. (35) and (37) can be computed beforehand for sufficiently small intervals of the axle position x_k and the values of the resulting matrix elements can be linearly interpolated during the evaluation of Eq. (30) to increase the computational efficiency.

4. Coupled equations of the train-track-bridge-soil system

In the next step, the system equations of the track-bridge-soil subsystem, Eq. (30), and the equations of motion of the train, Eq. (12), are combined into one set of equations,

$$\mathbf{M}^*(t)\ddot{\mathbf{x}}^*(t) + \mathbf{C}^*(t)\dot{\mathbf{x}}^*(t) + \mathbf{K}^*(t)\mathbf{x}^*(t) = \mathbf{f}^*(t) \tag{44}$$

with

$$\mathbf{M}^* = \mathrm{diag}[\mathbf{M}_B, \mathbf{M}_c], \quad \mathbf{C}^* = \mathrm{diag}[\mathbf{C}_B, \mathbf{C}_c], \quad \mathbf{K}^* = \mathrm{diag}[\mathbf{K}_B, \mathbf{K}_c]$$

$$\mathbf{x}^*(t) = \begin{bmatrix} \mathbf{h}_B \\ \mathbf{u}_c \end{bmatrix}, \quad \mathbf{f}^*(t) = \begin{bmatrix} \mathbf{f}_B \\ \mathbf{f}_c \end{bmatrix} \tag{45}$$

In this system of equations, however, the DOFs at the interface of the two subsystems are not independent of each other. The coupling of these DOFs is achieved with the so-called *corresponding assumption* [40–42], which assumes a constant rigid-body contact between the axles of the train and the underlying rail and thus does not allow any lift-off of the axles (compare with Figs. 1 and 4). In addition, within the framework of the *corresponding assumption*, track irregularities can also be taken into account by introducing a random irregularity profile function I_{irr} superimposed on the vertical track displacement [42]. Therefore, for the vehicle-bridge interaction problem considered, the vertical axle displacement u_{ak} is equal to the deflection w_r of the track plus that of the track irregularity profile function I_{irr} at the position x_k of the train axle. When w_r is divided into $w_r^{(f)}$ and $w_r^{(b)}$ according to Eq. (18), $w_r^{(f)}$ replaced by Eq. (19) and the series expansion Eq. (20) used for $w_r^{(b)}$, the following relationship between the coupled DOFs of the vehicle and the track is obtained,

$$u_{ak}(x_k) = w_r(x_k, t) + I_{irr}(x_k)$$

$$\approx y_{rk}(t) + \sum_{m=1}^{N_b} \Psi_r^{(m)}(x_k)y_b^{(m)}(t) + \sum_{m=1}^{N_b} \bar{\Psi}_r^{(m)}(x_k)\bar{y}_b^{(m)}(t) + I_{irr}(x_k) \tag{46}$$
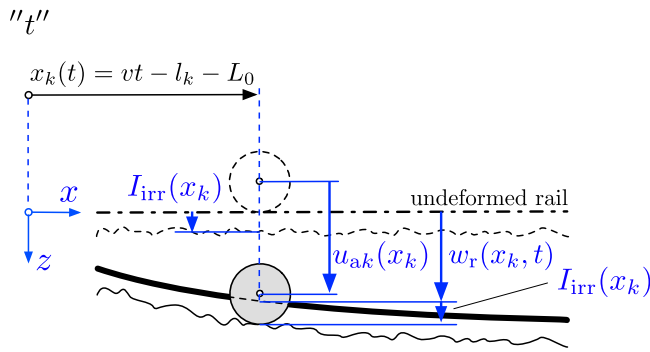
$''t''$

Fig. 4. Corresponding assumption for the axle at position x_k.
Source: Modified from [12].

The function I_{irr} can be generated from power spectral density functions of measured track irregularities, as discussed in [43]. The onefold and twofold derivative of this relation with respect to time gives the axle velocity and axle acceleration, respectively, as specified in *Appendix C* (Eqs. (C.1) and (C.2)). Furthermore, according to the *corresponding assumption*, the interaction forces between the track and the vehicle are equal, i.e. the kth axle load $F_{\mathrm{a}k}$ corresponds to the interaction force F_k on the track.

Based on the relationship Eq. (46) between the DOFs of both subsystems and its first and second derivatives with respect to time, Eqs. (C.1) and (C.2), a DST can now be applied that condenses in Eq. (44) the DOFs of the train axles to the coordinates of the coupled track-bridge-soil subsystem. This condensation leads to the following relationship between the vector of the DOFs of the two decoupled subsystems $\mathbf{x}^*(t)$ and the vector of the condensed DOFs of the coupled system after condensation $\tilde{\mathbf{u}}_{\mathrm{c}}$ (i.e., without the DOFs of the axle displacement), and their velocities and accelerations,

$$\mathbf{x}^*(t) = \boldsymbol{\Gamma}(t)\mathbf{x}(t) + \boldsymbol{Y}(t),$$

$$\dot{\mathbf{x}}^*(t) = \dot{\boldsymbol{\Gamma}}(t)\mathbf{x}(t) + \boldsymbol{\Gamma}(t)\dot{\mathbf{x}}(t) + \dot{\boldsymbol{Y}}(t), \qquad \mathbf{x}(t) = \begin{bmatrix} \mathbf{h}_{\mathrm{B}} \\ \tilde{\mathbf{u}}_{\mathrm{c}} \end{bmatrix}, \qquad (47)$$

$$\ddot{\mathbf{x}}^*(t) = \ddot{\boldsymbol{\Gamma}}(t)\mathbf{x}(t) + 2\dot{\boldsymbol{\Gamma}}(t)\dot{\mathbf{x}}(t) + \boldsymbol{\Gamma}(t)\ddot{\mathbf{x}}(t) + \ddot{\boldsymbol{Y}}(t)$$

with the time-dependent transformation matrix $\boldsymbol{\Gamma}(t)$ defined in Appendix C, which results from the compatibility condition of Eq. (46), and $\boldsymbol{Y}(t)$ including the values of the track irregularity profile function I_{irr} at the axle positions. Eq. (47) is now substituted into the system of equations of the two subsystems, Eq. (44), and pre-multiplied by $\boldsymbol{\Gamma}^{\mathrm{T}}(t)$. This finally leads to the coupled set of equations of motion for the interacting train-track-bridge-ground system,

$$\mathbf{M}(t)\ddot{\mathbf{x}}(t) + \mathbf{C}(t)\dot{\mathbf{x}}(t) + \mathbf{K}(t)\mathbf{x}(t) = \mathbf{f}(t) \qquad (48)$$

with

$$\begin{aligned}
\mathbf{M}(t) &= \boldsymbol{\Gamma}^{\mathrm{T}}(t)\mathbf{M}^*(t)\boldsymbol{\Gamma}(t), \\
\mathbf{C}(t) &= \boldsymbol{\Gamma}^{\mathrm{T}}(t)\left(\mathbf{C}^*(t)\boldsymbol{\Gamma}(t) + 2\mathbf{M}^*(t)\dot{\boldsymbol{\Gamma}}(t)\right), \\
\mathbf{K}(t) &= \boldsymbol{\Gamma}^{\mathrm{T}}(t)\left(\mathbf{K}^*(t)\boldsymbol{\Gamma}(t) + \mathbf{C}^*(t)\dot{\boldsymbol{\Gamma}}(t) + \mathbf{M}^*(t)\ddot{\boldsymbol{\Gamma}}(t)\right), \\
\mathbf{f}(t) &= \boldsymbol{\Gamma}^{\mathrm{T}}(t)\left(\mathbf{f}^*(t) - \mathbf{M}^*(t)\ddot{\boldsymbol{Y}}(t) - \mathbf{C}^*(t)\dot{\boldsymbol{Y}}(t) - \mathbf{K}^*(t)\boldsymbol{Y}(t)\right)
\end{aligned} \qquad (49)$$

Since the dynamic interaction forces $F_{\mathrm{a}k}(t)$ and F_k cancel each other out when $\mathbf{f}^*(t)$ is pre-multiplied by $\boldsymbol{\Gamma}^{\mathrm{T}}(t)$, only the static axle loads (Eqs. (15) and (14)) contribute to the force vector $\mathbf{f}(t)$. The numerical solution of Eq. (49) can be found by applying the Newmark-β method.

4.1. Track irregularities

Especially for trains moving at high speeds track irregularities become a major source of excitation. These geometrical imperfections, represented by the random irregularity profile function $I_{\mathrm{irr}}(x)$ in Eq. (49), can be understood as a stationary stochastic process in space [3]. Such a random irregularity profile function can be realized by a stochastic superposition of J harmonic functions with discrete spacial circular frequencies Ω_n ($n = 1, \ldots, J$) and the random phase angle φ_n, which is uniformly distributed in the range $0 \leq \varphi_n \leq 2\pi$ [43],

$$I_{\mathrm{irr}}(x) = \sqrt{2} \sum_{n=1}^{J} A_n \cos(\Omega_n x + \varphi_n) \qquad (50)$$

The frequency increment $\Delta\Omega = (\Omega_{\mathrm{u}} - \Omega_{\mathrm{l}})/J$ is defined by the upper frequency bound Ω_{u} and the lower frequency bound Ω_{l} respectively. The amplitude A_n is derived from [44]

$$A_n = \sqrt{\frac{S(\Omega_n)}{\pi}\Delta\Omega} \qquad (51)$$

Herein, the two-sided power spectral density $S(\Omega_n)$ is represented by the one-sided power spectral density function $\Phi_{\mathrm{v}}(\Omega_n)$ [43]

$$S(\Omega_n) = \frac{\Omega_n}{2}, \quad \Omega_n = Q\frac{\Omega_{\mathrm{c}}^2}{(\Omega_{\mathrm{r}}^2 + \Omega_n^2)(\Omega_{\mathrm{c}}^2 + \Omega_n^2)} \qquad (52)$$

with $\Omega_{\mathrm{r}} = 0.0206$ rad/m and $\Omega_{\mathrm{c}} = 0.8246$ rad/m, respectively. The amplitude Q defines the overall quality of the track, reaching from $Q = 5.923 \cdot 10^{-7}$ m for a good quality track, to $Q = 15.861 \cdot 10^{-7}$ m for a poor quality track.

5. Application

5.1. Validation

As the proposed modeling strategy introduced some simplifying assumptions, the resulting response prediction is compared to that of an FE model of an example bridge. For this validation, the proposed semi-analytical approach is implemented in MATLAB [45], whereas the FE model is created using the software suite Abaqus [46]. The example bridge is selected to represent a steel bridge of length $L_{\mathrm{b}} = 17.5$ m, with the flexural rigidity $EI_{\mathrm{b}} = 1.356\cdot10^{10}$ N m^2 and the mass per unit length $\rho A_{\mathrm{b}} = 7083$ kg/m. The rails used in the present study are two UIC60 rails with the combined mass per unit length $\rho A_{\mathrm{r}} = 120.733$ kg/m and the combined flexural rigidity $EI_{\mathrm{r}} = 12.831\cdot10^6$ N m^2 [47]. The stiffness coefficient $k_{\mathrm{f}} = 104 \cdot 10^6$ N/m^2 and the damping parameter $c_{\mathrm{f}} = 50$ kN s/m^2 are selected to represent a ballast of low stiffness [47]. The length of the track before and after the bridge bearings is $L_0 = 30$ m, and thus considerably larger than the minimum length of 5.27 m according to Eq. (1). The subsoil considered is of moderate stiffness with the constrained modulus $E_{\mathrm{s}} = 2.5\cdot10^8$ N/m^2, the *Poisson*'s ratio $\nu = 0.28$ and the density $\rho_{\mathrm{s}} = 2300$ kg/m^3. The mass of the foundation is $\tilde{m}_1 = 2.5\cdot10^5$ kg with an assumed foundation surface area $A_0 = 40$ m^2. Based on the cone model of Wolf the resulting parameters representing the soil and foundation properties (cf. Fig. 1) are $k_{\mathrm{b}} = 1.514\cdot10^9$ N/m, $c_{\mathrm{b}} = 3.033\cdot10^7$ N s/m and $m_{\mathrm{b}} = \tilde{m}_1 = 2.5\cdot10^5$ kg. For the present investigation, random track imperfections generated according to Eq. (50) are considered. To this end the amplitude for a poor quality track $Q = 15.861 \cdot 10^{-7}$ m is chosen, and the range of the $J = 1000$ spacial frequencies is restricted by the boundaries $\Omega_{\mathrm{l}} = \pi/50$ m^{-1} and $\Omega_{\mathrm{u}} = \pi$ m. The track irregularity profile generated in this manner is shown in Fig. 5.

The same model parameters are used in the FE model, with both the bridge and the track girder discretized as Euler–Bernoulli beam elements (B23) with the uniform element length of 6.125 cm. In this model, the track is modeled as a finite beam, with simply supported ends, placed at a distance of $L_0 = 30$ m before and after the supports of the bridge. The deviation of the track geometry from the perfectly straight and smooth track is modeled by simply offsetting the element nodes perpendicular to the beam axis by the amount of the irregularity profile (cf. Fig. 5) at each nodal position x.

For the vehicle, a simple two DOF model is considered, moving at a constant speed of $\upsilon = 70$ m/s (cf. Fig. 6). The parameters shown in Fig. 6 are selected to represent the MSD system corresponding to
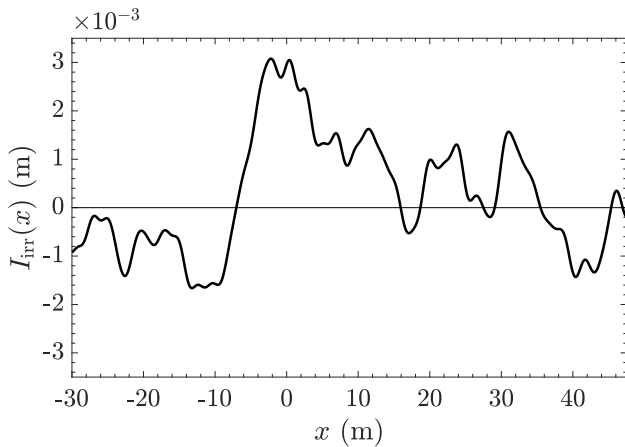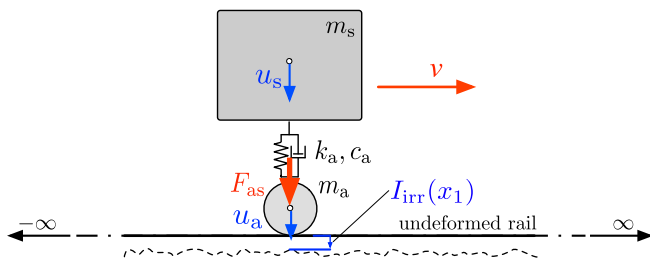
Fig. 5. Irregularity profile of the track.

Fig. 6. Two degree of freedom vehicle system.
Source: Modified from [28].

a single axle of the ICE3 train model. The system matrices $\mathbf{M}_c$, $\mathbf{C}_c$, $\mathbf{K}_c$, the force vector $\mathbf{F}_c$, and the vector of DOFs $\mathbf{u}_c$ of Eq. (12) read as

$$\mathbf{M}_c = \begin{bmatrix} m_s & 0 \\ 0 & m_a \end{bmatrix}, \quad \mathbf{C}_c = \begin{bmatrix} c_a & -c_a \\ -c_a & c_a \end{bmatrix}, \quad \mathbf{K}_c = \begin{bmatrix} k_a & -k_a \\ -k_a & k_a \end{bmatrix}$$
$$\mathbf{F}_c = \begin{bmatrix} 0 \\ F_{as} \end{bmatrix}, \quad \mathbf{u}_c = \begin{bmatrix} u_s \\ u_a \end{bmatrix} \tag{53}$$

Therefore, the mass m_s = 15125 kg represents the combined mass of half a bogie and one quarter of the car-body, and m_a = 1800 kg denotes the mass of a single axle [28,48]. The suspension stiffness and damping coefficients are k_a = 1.764 MN/m and c_a = 48 kN s/m, respectively [28,48]. In the proposed approach, this system is coupled to the rail according to the previously discussed *corresponding assumption*. In the FE model, the coupling is realized by defining a rigid contact between the axle and the rail beam.

In the computation of the dynamic response of the system based on the proposed semi-analytical approach, N_b = 8 modes of the bridge are considered. For the sake of comparison, computations with a stiffness coefficient of three times the reference stiffness ($3 \times k_f$ = 312 · 10^6 N/m²) are included to represent a ballast of high stiffness. The dynamic response of the FE model is calculated in a full transient analysis and represents the reference solution. Fig. 7(a) shows the displacement of the left support of the bridge (x = 0 m) and Fig. 7(b) the acceleration of the same point. At the beginning of the computation (t = 0 s), the MSD system enters the considered section ($-L_0 \leq x \leq L_b + L_0$) at $x = -L_0$ (cf. Figs. 1 and 3) until it leaves this section at $t \approx 1.107$ s. Therefore, $t = 0$ s corresponds to the time when the static axle load F_{as} (cf. Fig. 6) is switched on for the semi-analytical approach, and the axle is situated directly on top of the first support of the rail beam of the FE model. Within this time frame, the MSD system arrives at the first support of the bridge at $t_B \approx 0.429$ s and leaves the bridge at $t_C \approx 0.679$ s. As can be seen, the results of the FE solution, represented by the black dashed line, are in excellent agreement with the results of

the proposed model, represented by the red line. This is also the case for the solutions including a higher value of the ballast stiffness since the dotted line representing the FE solution is in excellent agreement with the corresponding results of the proposed model, represented by the green line. It should also be noted that no influence of the boundary condition of the rail beam at $x = -L_0$ is observed on the dynamic response of the bridge support and the load-distributing effect of the track is well approximated by the proposed model. Since higher ballast stiffness results in a more concentrated load distribution, the acceleration peak observed at the time where the axle arrives at the left bridge support is of greater value, as visible from the comparison of the results with higher ballast stiffness ("$3 \times k_f$") to the results with lower stiffness.

Fig. 8(a) shows the bridge displacement and Fig. 8(b) the bridge acceleration at the quarter point ($x = L_b/4 = 4.375$ m) of the bridge. This position is specifically selected because the biggest impact of the track irregularities on the dynamic response of the bridge is observed here. Both the deflection and the acceleration at this point are significantly higher than at the supports. While the influence of ballast stiffness on the deflection is small at this point, the computed accelerations vary significantly. The accelerations resulting from a ballast of lower stiffness are significantly higher than the ones computed with a stiffer ballast. It should be noted that the results of the proposed model are again in excellent agreement with the solution of the FE model, regardless of the ballast stiffness coefficient used.

Since the movement of the axle mass together with the coupled track can significantly influence the dynamic response of the bridge when track irregularities are considered [28], the vertical displacement of the axle u_a is depicted in Fig. 9(a) and its acceleration in the vertical direction $\ddot{u}_a$ in Fig. 9(b). As can be seen, the different boundary conditions of the two track models result in a notable difference in the computed displacement as well as the acceleration of the two models at the beginning of the computation. This brief transient phase does, however, not affect the bridge response. After this brief phase, the response histories of the two models are in good agreement, further validating the proposed semi-analytical approach. It can also be seen, that a larger ballast stiffness results in a smaller vertical displacement of the axle. As previously observed for the accelerations of the bridge, a smaller value of the ballast stiffness is associated with greater accelerations of the wheel.

For a fixed time step of $\Delta t = 10^{-4}$, the computation time of the proposed semi-analytical model was 47.51 s, while the computation time of the FE model was 2043 s on the same hardware. Most of the computation time (44.17 s) was spent on the initial computation of the natural frequencies, eigenfunctions, and shape functions, while only 3.34 s was spent on the computation of the time history of the response.

5.2. Exemplary application

The now validated approach is used in the following to analyze the dynamic response of an example bridge subjected to high-speed trains. For this purpose, the same steel bridge as before is considered with the same parameters. The first six complex natural frequencies of this bridge model and their respective equivalent damping ratios are listed in Table 1. As also observed in [6,28], two highly damped modes ($m = 2$ and $m = 3$) occur for the present subsystem of the bridge on subsoil. The damping of these modes is high because the absolute value of the real part of s_b is very close to the imaginary part of s_b. From Eq. (A.5) it follows that $\zeta_b^{(m)}$ reaches an upper bound of 100% when the absolute real and imaginary parts of the complex natural frequency s_b coincide. In Table 1 also the corresponding natural frequencies $f_b^{(m)} = \Im(s_b^{(m)})/(2\pi) = \Omega_b^{(m)}/(2\pi)$ are listed. For comparison, the first six natural frequencies of the bridge on rigid supports $f_{b,rigid}^{(m)}$, with [4]

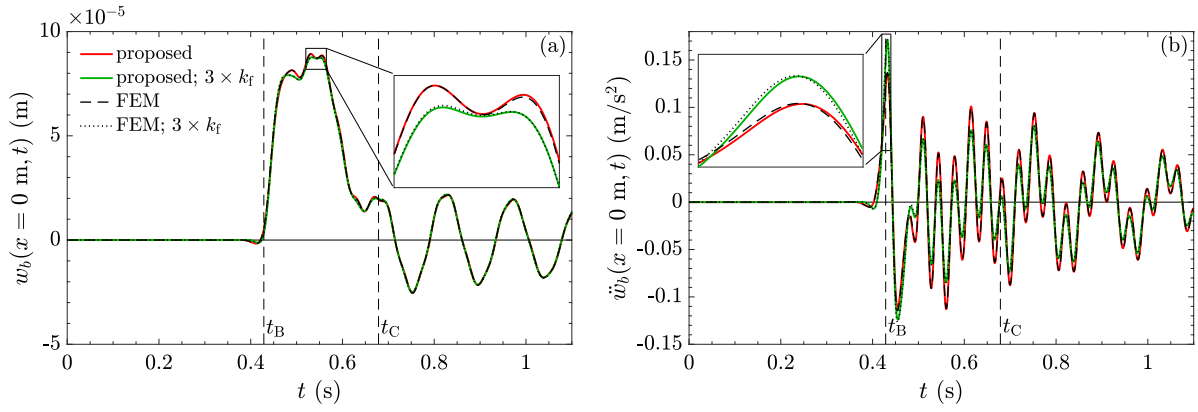$$f_{b,rigid}^{(m)} = \left(\frac{m}{L_b} \right)^2 \frac{\pi}{2} \sqrt{\frac{E I_b}{\rho A_b}} \tag{54}$$

Fig. 7. (a) Bridge deflection and (b) acceleration at the left support ($x = 0$). (For interpretation of the references to color in this figure legend, the reader is referred to the web version of this article.)
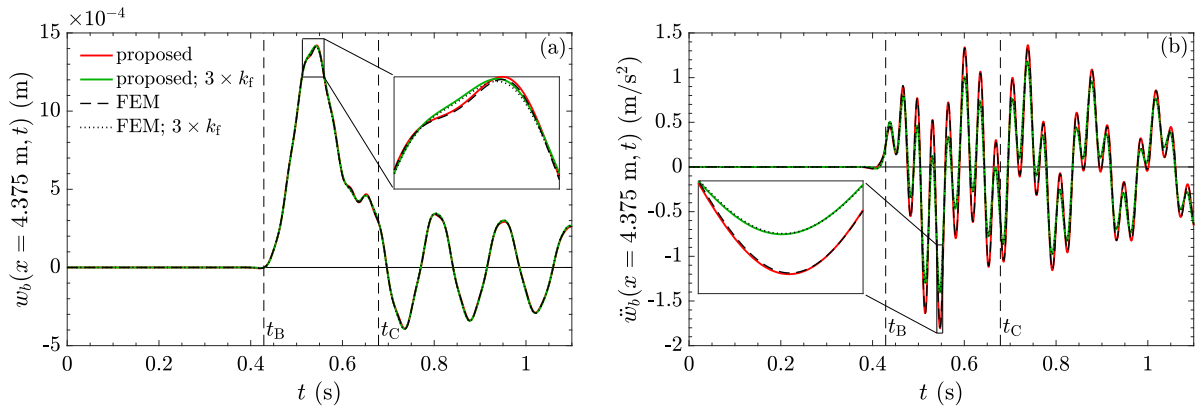

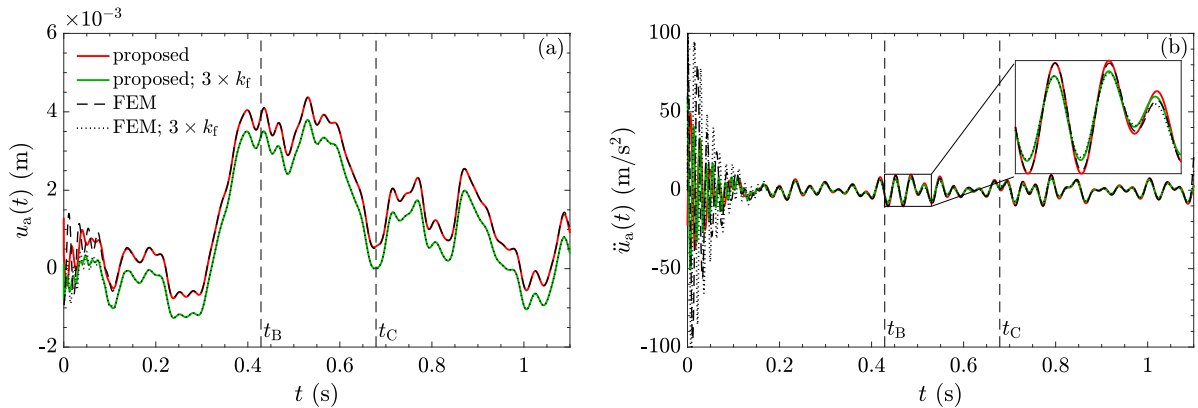**Fig. 8.** (a) Bridge deflection and (b) acceleration at the position $x = 1/4 L_b = 4.375$ m.

Fig. 9. (a) Axle displacement and (b) acceleration.

are specified in the last column. As can be seen, the integration of the soil–structure interaction in this simplified model leads to a reduction of the first natural frequency compared to the rigidly supported case. Additionally, modes two and three appear only in the flexibly supported beam, while the fourth mode is similar to the second mode of the rigidly supported case. The fourth and higher modes of the flexibly supported bridge, however, have a slightly larger natural frequency than the corresponding modes of the rigidly supported bridge.

To further investigate the response prediction based on the proposed model, the response of the considered bridge to the passage of a standard ICE3 train model is discussed. To account for the structural damping of the bridge, to each of the $N_b = 8$ modes ($m = 1, \ldots, N_b$),

a modal damping ratio of $\tilde{\xi}_b^{(m)} = 0.5\%$ is added to the damping ratio resulting from the dashpots located below the supports. This modal damping ratio corresponds to the base value of the applicable modal damping ratio of steel bridges defined in [49].

The $N_c = 8$ equal vehicles of the ICE3 train are described by the mechanical model with ten DOFs according to Section 2.3. The corresponding masses (m_p, m_s, m_a), moments of inertia (I_p, I_s), stiffness coefficients (k_s, k_a), damping coefficients (c_s, c_a), and dimensions ($h_a^{(j)}$, $h_s^{(j)}$) of this model can be found in [28,48].

In this study, the dynamic response of the bridge due to the passing train is computed with 81 different train speeds. These speeds are evenly distributed in the range from 10 to 90 m/s. For each one of
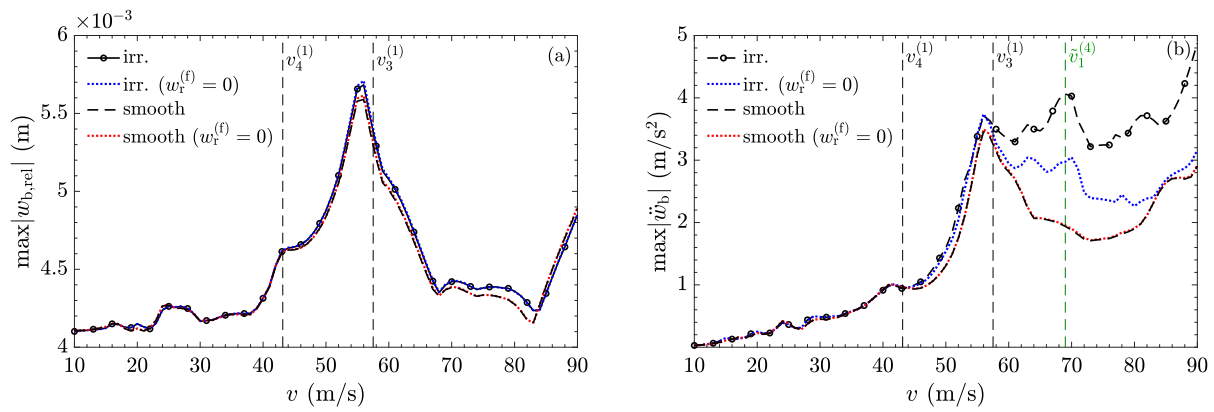
Fig. 10. Bridge response with and without track irregularities; Effect of the track response on the bridge response. (a) Peak bridge deflection and (b) peak bridge acceleration. (For interpretation of the references to color in this figure legend, the reader is referred to the web version of this article.)

Table 1
Complex natural frequencies of the first six modes of the considered bridge-soil subsystem, together with the corresponding natural frequency and equivalent damping ratio. Last column: natural frequencies of the bridge on rigid supports.

Mode m	Compl. nat. frequency $s_b^{(m)}$ (rad/s)	Damping ratio $\zeta_b^{(m)}$ (%)	nat. frequency $f_b^{(m)}$ (Hz)	nat. frequency $f_{b,rigid}^{(m)}$ (Hz)
1	$-1.03 + 43.76i$	2.36	6.96	7.10
2	$-56.21 + 49.97i$	74.74	7.95	28.39
3	$-56.92 + 52.62i$	73.42	8.38	63.87
4	$-2.54 + 181.64i$	1.40	28.91	113.55
5	$-1.25 + 405.46i$	0.31	64.53	177.42
6	$-0.72 + 717.77i$	0.10	114.24	255.48

these train speeds, the maximum absolute relative bridge deflection,

$$\max \left| w_{b,rel} \right| = \max \left| w_b(x,t) - (w_b(0,t) + x(w_b(L_b,t) - w_b(0,t))/L_b) \right| \quad (55)$$

and the maximum absolute acceleration, $\max \left| \ddot{w}_b \right|$, are computed and stored. Herein, the bridge response is evaluated using a spatial sampling with 101 points uniformly distributed over the interval [0, 17.5], with the first and last points located at the supports of the bridge. Plotting the peak response against the corresponding train speed yields the response spectra depicted in Fig. 10(a) and (b), with the black line with markers referring to the outcomes of the proposed semi-analytical model considering rail irregularities ("irr.") according to the profile illustrated in Fig. 5. The response without the response portion $w_r^{(f)}$ (i.e. $w_r^{(f)} = 0$) is shown in a blue dotted line. Additionally, the results of the model without track irregularities are shown with a black dashed line (full model) and a red dotted line ($w_r^{(f)} = 0$), respectively. As can be seen in Fig. 10(a), the track irregularities have only a small influence on the computed bridge *deflection*. The deflection with and without track irregularities only start to diverge visibly from each other at a train speed of 45 m/s. Furthermore, it can be seen that $w_r^{(f)}$ has only a very small negligible contribution to the dynamic deflection, whether the model is considered with or without rail irregularities.

For *acceleration*, however, the response behavior is different, see Fig. 10(b). Firstly, it can be observed that from a train speed of about 55 m/s, the solutions with and without track irregularities differ significantly. In this speed range, the maximum acceleration of the model with track irregularities is considerably larger. Furthermore, it can be seen that the response component $\ddot{w}_r^{(f)}$ is very substantial when track irregularities are present. This observation highlights the importance of including the dynamic track substructure when geometric imperfections are considered and bridge accelerations are of interest [28]. In contrast, for a bridge with a smooth track, this response component plays no role in the maximum acceleration, i.e. the red dotted line and the black dashed line agree with each other in the entire speed range considered.

Both in the spectral representation of the deflection and the acceleration, resonance peaks can be observed which occur at certain train speeds. In Fig. 10(a) and (b) they are indicated by vertical dashed lines. Here, the black vertical lines indicate second order resonant speeds $v_i^{(m)}$ [13,40,50],

$$v_i^{(m)} = \frac{d_c f^{(m)}}{i} \quad (56)$$

which are related to the regular pattern of the axial forces ($m = 1, \ldots, N_b$, $i = 1, 2, \ldots$). The distance d_c is the vehicle length and, therefore, the distance of the regular spacing of the axle loads. For the present ICE3 train model, this constant is $d_c = 24.775$ m. For the first bridge mode ($m = 1$), two corresponding resonance speeds are $v_3^{(1)} = 57.51$ m/s and $v_4^{(1)} = 43.13$ m/s.

At first sight, it could be concluded that the third vertical line in Fig. 10 corresponds to a resonant speed related to the third mode of the bridge (i.e. $v_3^{(3)} = 69.18$ m/s). However, since this mode is one of the two highly damped modes ($\zeta_b^{(m)} = 73.42\%$), no significant response amplification at resonance is expected. Furthermore, the observation that the resonance peak in the acceleration response only occurs in the presence of track irregularities makes amplification by a third-order resonance speed [40],

$$\tilde{v}_i^{(m)} = \frac{\tilde{\lambda} f^{(m)}}{i} \quad (57)$$

a likely explanation. In Eq. (57), $\tilde{\lambda}$ represents the dominant wave length of the irregularities. Since the wavelengths used to generate the irregularity profile according to Eq. (50) are distributed at constant frequency intervals between the limits $\tilde{\lambda}_{min} = 2\pi/\Omega_u = 2$ m and $\tilde{\lambda}_{max} = 2\pi/\Omega_l = 100$ m, the dominant wavelength is not known a priori. However, from the observation that the maximum acceleration at the train speed $v \approx 69$ m/s occurs at the quarter point of the bridge ($x = 1/4L_b$), resonance with the fourth mode ($m = 4$), which has its maximum at the same point, is the likely explanation. Inserting $m = 4$ and $i = 1$ together with $v_1^{(4)} = 69$ m/s gives the dominant wavelength $\tilde{\lambda} = 2.39$ m. However, since the considered wavelengths are equally distributed between the specified limits, the dynamic amplification may not be contributed to the single wavelength $\tilde{\lambda}$. Moreover $\tilde{\lambda} = 2.39$ m suggests a greater influence of shorter wave lengths, close to the lower limit of $\tilde{\lambda}_{min} = 2$ m. Due to the 32 consecutive axle loads of the $N_c = 8$ vehicles acting on the bridge, the maximum absolute acceleration observed at $v \approx 69$ m/s in Fig. 11 is significantly higher than the accelerations observed in Fig. 8, resulting from a single axle.

In the next study, the results of the semi-analytical approach proposed here are compared with the model using modal expansion of the track response $w_r^{(f)}$, as described in [29]. In a convergence study of the latter model, the number of modes N_r for the approximation of $w_r^{(f)}$ is varied in the presence of track irregularities. Fig. 11 shows
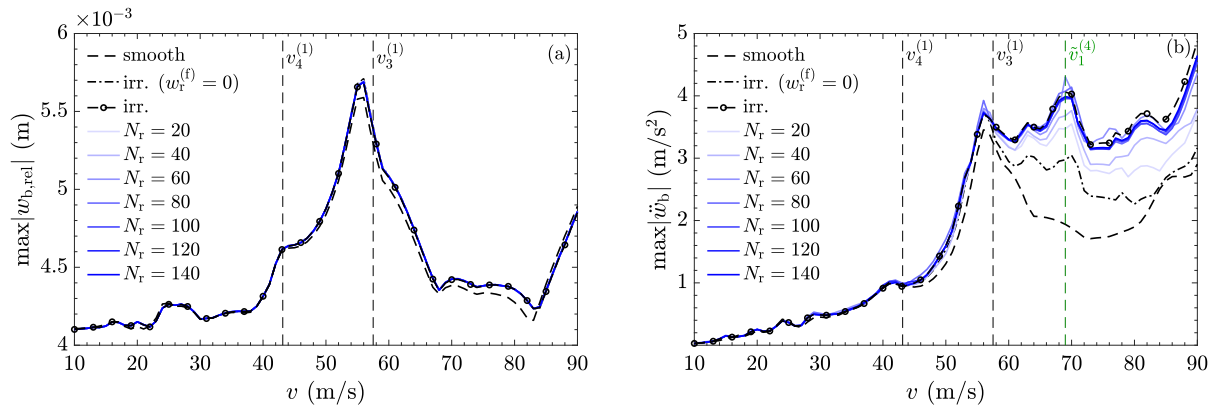
Fig. 11. Response according the proposed approach vs. the approach based on modal expansion of the track substructure. (a) Peak bridge deflection and (b) peak bridge acceleration.
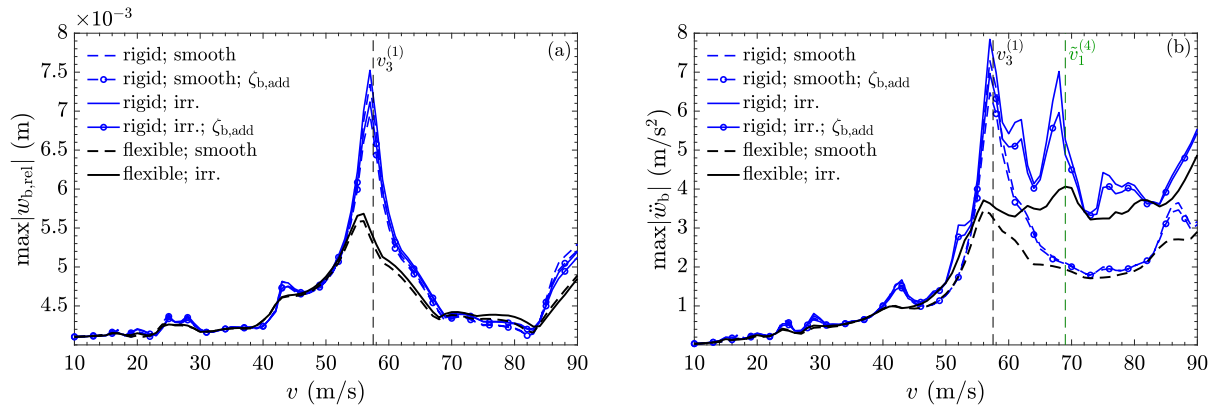

Fig. 12. Response of the flexibly supported and the rigidly supported bridge. (a) Peak bridge deflection and (b) peak bridge acceleration.

the maximum deflection (left) and maximum acceleration (right) as a result of the considered approaches. As expected after the previous considerations, the number of modes to approximate $w_r^{(f)}$ do not play a role in the deflection, as this response fraction is very small, Fig. 11(a).

In contrast, however, the bridge acceleration depends very much on the number of track modes considered. When 40 track modes are used in the model based on modal expansion of the bridge, the bridge acceleration is strongly underestimated, as can be seen in Fig. 11(b). With 80 modes, the maximum acceleration is better approximated, but at the cost of overestimating accelerations at resonant speeds $v_3^{(1)}$ and $v_3^{(4)}$, while at higher train speeds accelerations are underestimated compared to the proposed semi-analytical approach and when calculated with more than 80 modes. The acceleration spectra based on 100, 120 and 140 track modes differ only slightly, with the acceleration increasing slightly when more modes are considered. The predicted accelerations of the proposed semi-analytical approach tend to be slightly higher than those of the model with the maximum number of track modes ($N_r = 140$), resulting in a conservative approximation of the response. In summary, the results of the proposed semi-analytical strategy agree very well with those of the modal superposition of the track modes also used in [28]. As discussed for Fig. 11, an initial convergence study is necessary in case of modal superposition of $w_r^{(f)}$. It should also be noted, that, as the number of track modes increased, a decrease of the time step was necessary to achieve numerical stability, adding to the computational time necessary. Overall, the proposed strategy shows high computational robustness as it does not depend on initial convergence studies for choosing an appropriate number of track modes, making it suitable for extensive parametric studies and stochastic simulations, as in [25].

Eventually, the main motivation behind the presented approach should be addressed, namely the computational efficiency. The number

of DOFs considered is given by the number of complex bridge modes and their respective complex conjugates, $2N_b$, the number of isolated *Rayleigh–Ritz* approximations corresponding to the number of axes, N_a, and the number of internal DOFs of the train, $6N_c$, yielding a total of 96 DOFs considered in Eq. (48). While the model used in [28] also has good computational efficiency, it requires of 264 DOFs to obtain reliable results (i.e. $N_r = 100$). For a comparison of computational efficiency, the response spectrum, derived from the 81 consecutive time–history computations (cf. Figs. 10 and 11) was computed with a constant time step of $\Delta t = 3.9 \cdot 10^{-4}$ s, for the proposed model, as well as the model of [28] in which $N_r = 100$ track modes were used. For the proposed model, the computational time needed was 6456 s, while the model of [28] took 98 334 s on the same hardware. Albeit noting that these computation times highly depend on the individual implementation of the code, the efficiency of the proposed model is clearly visible from this simple comparison. Also, it has to be noted that the limiting factor for the chosen time step of $\Delta t = 3.9 \cdot 10^{-4}$ s was the convergence of the model based on modal expansion [28] since greater time increments lead to convergence issues. However, for the proposed model, an increase of this time step did not lead to a decreased convergence, and for $\Delta t = 7.8 \cdot 10^{-4}$ s lead to the same response spectra, thus further decreasing the computational time needed by a factor of two.

To further illustrate the significant influence of the soil–structure interaction on the system response, Fig. 12 compares the response of a pinned–pinned beam model (i.e. the soil is assumed to be rigid) with that of the considered flexibly supported structural model (shown in Figs. 10 and 11). Again, computations were performed with an irregular track according to Fig. 5 and alternatively with a perfectly straight and smooth track. For both the rigidly and flexibly supported bridge (denoted by "$\zeta_{b,add}$"), a base value of the modal damping ratio of $\tilde{\zeta}_b^{(m)} =$

0.5% was assigned to each mode. Since the span is less than 20 m, in the pinned–pinned bridge model the modal damping ratio was increased by $\tilde{\zeta}_{b,add} = 0.125(20 - L_b) = 0.3125\%$ as suggested in [49] to indirectly account for the soil–structure interaction. This additional damping yields a significant reduction of the deflection and acceleration peaks close to the second order resonance speed $v_3^{(1)} = 57.51$ m/s as can be seen in Fig. 12, where also the peak response of the pinned–pinned beam without additional damping is illustrated. For the computations that also take into account the irregularity profile, this reduction is also present for the acceleration at the third order resonant speed of $\tilde{v}_1^{(4)} = 69$ m/s. Comparing the deflections and accelerations of the rigidly supported bridge with those of the bridge on flexible supports reveals that in the latter model the response peaks at resonance are substantially smaller. The reason for this is that the modal damping ratios resulting from the non-proportional damping of the elastically supported beam have a significant order of magnitude (cf. Table 1). Since the modal damping ratio of the first mode is significantly higher than the modal damping ratio of the fourth mode, the acceleration response at $v_3^{(1)}$ is reduced more, and the peak at $\tilde{v}_1^{(4)}$ is larger than that at $v_3^{(1)}$ for the bridge on flexible supports including the track irregularities.

6. Summary and conclusions

In this contribution, a novel semi-analytical approach to predict the dynamic responses of railway bridges was presented, which allows considering the interaction between the vehicle, the track, the bridge, and the underlying soil in a simplified manner. The coupling of the mass–spring–damper system of the train with the underlying system of the track and the bridge-soil was achieved by a dynamic substructuring procedure based on the *corresponding assumption*. As a novelty, this approach combines the complex modal representation of the non-classically damped bridge-soil model with a *Rayleigh–Ritz* approximation of the deflection of the infinitely long track beam on viscoelastic bedding. This methodology takes advantage of the strongly isolated deflection shape of the rails around the axles, which is otherwise the reason for the large number of modes that are needed when the track response is modally expanded.

Based on the application example shown, the following conclusions can be drawn for the dynamic system under consideration consisting of the train, track, bridge, and subsoil:

- The proposed model accurately predicts the load-distributing effects of the track on the acceleration response as well as the influence of the track response on the bridge deflection and acceleration. This excellent agreement is attributed to the good approximation of the dynamic response of the axle mass in combination with the coupled track.
- The predicted bridge acceleration is strongly influenced by the presence of rail irregularities. This influence is significantly amplified by the dynamic response of the track in combination with the mass of the train axles.
- Consideration of soil–structure interaction can have an important influence on the dynamic response. This influence is particularly large at resonance speeds, as can be concluded from the substantial reduction in deflection and acceleration peaks. Since the soil–structure interaction results in different damping for each mode of the bridge, this reduction in resonance peaks depends on the corresponding mode number.
- The modeling approach allows for a simple yet accurate response prediction that far exceeds the computational efficiency of comparative finite element models.

CRediT authorship contribution statement

Paul König: Methodology, Software, Validation, Formal analysis, Investigation, Writing – original draft. **Patrick Salcher:** Methodology, Supervision. **Christoph Adam:** Conceptualization, Resources, Writing – review & editing, Supervision.

Declaration of competing interest

The authors declare that they have no known competing financial interests or personal relationships that could have appeared to influence the work reported in this paper.

Appendix A. Modal parameters and orthogonality relations of the bridge-soil model

First, the general form of the eigenfunctions of the non-classically damped Euler–Bernoulli beam [31,51]

$$\Phi_b(x) = C_1 \sin \frac{\lambda_b x}{L_b} + C_2 \cos \frac{\lambda_b x}{L_b} + C_3 \sinh \frac{\lambda_b x}{L_b} + C_4 \cosh \frac{\lambda_b x}{L_b} \tag{A.1}$$

are substituted into the four boundary conditions (Eq. (10)), which yields a homogeneous set of four equations. By zeroing the corresponding coefficient determinant, the eigenvalues $\lambda^{(m)}$ ($m = 1, \ldots, \infty$) and their complex conjugates $\tilde{\lambda}^{(m)}$ are found. The mth eigenvalue $\lambda^{(m)}$ is related to the mth complex natural frequency $s^{(m)}$ by

$$\left(s_b^{(m)}\right)^2 = -\frac{\left(\lambda_b^{(m)}\right)^4}{L_b^4} \frac{E I_b}{\rho A_b} \tag{A.2}$$

which can be written as [52,53],

$$s_b^{(m)} = \sigma_b^{(m)} + i \Omega_b^{(m)} \tag{A.3}$$

Herein, the real part $\sigma_b^{(m)}$ is the so-called decay rate, and the imaginary part $\Omega_b^{(m)}$ is referred to as the damped natural frequency [54]. The absolute value of the complex natural frequency

$$\omega_b^{(m)} = \left|s_b^{(m)}\right| = \sqrt{\left(\sigma_b^{(m)}\right)^2 + \left(\Omega_b^{(m)}\right)^2} \tag{A.4}$$

is the so-called pseudo-undamped natural frequency. The mth modal equivalent damping ratio $\zeta^{(m)}$ is defined as [5]

$$\zeta_b^{(m)} = \frac{-\Re\left(s_b^{(m)}\right)}{\left|s_b^{(m)}\right|} = -\frac{\sigma_b^{(m)}}{\omega_b^{(m)}} \tag{A.5}$$

This equivalent modal damping ratio accounts for the non-classical damping of the bridge substructure, resulting from the discrete dashpots at the boundaries.

The modal damping ratio of (A.5) does not account for structural damping of the bridge, however, it can considered by simply adding the mth structural modal damping ratio $\tilde{\zeta}_b^{(m)}$, i.e. $\tilde{\zeta}_b^{(m)} + \zeta^{(m)}$ [12]. Then, the mth complex natural frequency can be expressed as

$$s_b^{(m)} = -\omega_b^{(m)}\left(\zeta_b^{(m)} + \tilde{\zeta}_b^{(m)}\right) + i\omega_b^{(m)}\sqrt{1 - \left(\zeta^{(m)} + \tilde{\zeta}^{(m)}\right)^2} \tag{A.6}$$

To derive the mth eigenfunction $\Phi_b^{(m)}$, the eigenvalues $\lambda_b^{(m)}$ are inserted into Eq. (A.1) and three of the four constants $C_1^{(m)}, C_2^{(m)}, C_3^{(m)}, C_4^{(m)}$ are expressed by the fourth, which can be scaled arbitrarily. The complex conjugate corresponding to the mth eigenfunction of the bridge

is referred to as $\bar{\Phi}_b^{(m)}$. The orthogonality relations of the non-classically damped Euler–Bernoulli beam can be found in [5,8,12]

$$
\begin{aligned}
a_b^{(m)} \delta_{lm} =& c_b \left(\Phi_b^{(m)}(0)\Phi_b^{(l)}(0) + \Phi_b^{(m)}(L_b)\Phi_b^{(l)}(L_b) \right) \\
&+ \left(s_b^{(l)} + s_b^{(m)} \right) \left(\rho_b A_b \int_0^{L_b} \Phi_b^{(m)}(x)\Phi_b^{(l)}(x)\mathrm{d}x \right. \\
&\left. + m_b \left(\Phi_b^{(m)}(0)\Phi_b^{(l)}(0) + \Phi_b^{(m)}(L_b)\Phi_b^{(l)}(L_b) \right) \right)
\end{aligned}
\tag{A.7}
$$

$$
\begin{aligned}
b_b^{(m)} \delta_{lm} =& k_b \left(\Phi_b^{(m)}(0)\Phi_b^{(l)}(0) \right. \\
&\left. + \Phi_b^{(m)}(L_b)\Phi_b^{(l)}(L_b) \right) + E I_b \int_0^{L_b} \Phi_{b,xx}^{(m)}(x)\Phi_{b,xx}^{(l)}(x)\mathrm{d}x \\
&- \left(s_b^{(m)} s_b^{(l)} \right) \left(\rho_b A_b \int_0^{L_b} \Phi_b^{(m)}(x)\Phi_b^{(l)}(x)\mathrm{d}x \right. \\
&\left. + m_b \left(\Phi_b^{(m)}(0)\Phi_b^{(l)}(0) + \Phi_b^{(m)}(L_b)\Phi_b^{(l)}(L_b) \right) \right)
\end{aligned}
\tag{A.8}
$$

Since the normalizing constants $a_b^{(m)}$ and $b_b^{(m)}$ are non-independent, they can both be expressed by the generalized modal mass [5,12]

$$
\begin{aligned}
M_b^{(m)} =& \frac{c_b}{2 s_b^{(m)}} \left(\left(\Phi_b^{(m)}(0) \right)^2 + \left(\Phi_b^{(m)}(L_b) \right)^2 \right) \\
&+ \rho_b A_b \int_0^{L_b} \left(\Phi_b^{(m)}(x) \right)^2 \mathrm{d}x + m_b \left(\left(\Phi_b^{(m)}(0) \right)^2 + \left(\Phi_b^{(m)}(L_b) \right)^2 \right)
\end{aligned}
\tag{A.9}
$$

in the form of $a_b^{(m)} = 2 s_b^{(m)} M_b^{(m)}$ and $b_b^{(m)} = -2 \left(s_b^{(m)} \right)^2 M_b^{(m)}$. The corresponding complex conjugates are represented by $\bar{a}_b^{(m)}$ and $\bar{b}_b^{(m)}$, respectively.

Appendix B. Approximation of the track substructure deflection

The *Rayleigh–Ritz* approximation of the response of the track beam on viscoelastic bedding due to the interaction forces with the train according to Eq. (19) is based on the shape function $\varphi_r(x - x_k(t))$, which moves with the corresponding interaction force. On the one hand, this shape function should represent the track deflection due to an inter-action force sufficiently accurate, but on the other hand it should be as simple as possible. Although the dynamic track deflection becomes asymmetric with increasing constant speed of the concentrated load, as observed in the steady-state solution of [4], it is assumed that the shape function φ_r in terms of the normalized symmetric static deflection due to a concentrated load

$$
\varphi_r(\hat{x}_k) = e^{-\beta \hat{x}_k}(\sin \beta \hat{x}_k + \cos \beta \hat{x}_k) , \quad \hat{x}_k \geq 0
$$
$$
\beta = \sqrt[4]{\frac{k_f}{4 E I_r}}
\tag{B.1}
$$

sufficiently approximates the actual dynamic track behavior, which is additionally influenced by track irregularities. In this equation, $\hat{x}_k(t) = x - x_k(t)$ denotes the local spacial coordinate starting at the kth axle position $x = x_k(t)$. In this study, this assumption has been confirmed in several application examples. The static deflection of the infinitely long bedded beam subjected to the concentrated force $F_k^{(\mathrm{stat})}$ at the position $\hat{x}_k$ reads [55]

$$
w_{rk}^{(f)(\mathrm{stat})}(\hat{x}_k) = \frac{F_k^{(\mathrm{stat})} \beta}{2 k_f} \varphi_r(\hat{x}_k) , \quad \hat{x}_k \geq 0
\tag{B.2}
$$

Once a suitable shape function has been identified, the *Rayleigh–Ritz* approximation for the kth interaction force, $w_{rk}^{(f)}(\hat{x}_k) = \varphi_r(\hat{x}_k)y_{rk}(t)$, is inserted into Eq. (2), in which quantities related to the deformation of the bridge-ground subsystem w_b and the other axle loads have been omitted. This leads to

$$
\begin{aligned}
& E I_r \varphi_{r,xxxx}(\hat{x}_k)y_{rk}(t) + \rho A_r \varphi_r(\hat{x}_k)\ddot{y}_{rk}(t) + c_f \varphi_r(\hat{x}_k)\dot{y}_{rk}(t) + k_f \varphi_r(\hat{x}_k)y_{rk}(t) \\
&= F_k(t)\delta(\hat{x}_k) \Pi(t, t_{Ak}, t_{Dk})
\end{aligned}
\tag{B.3}
$$

Pre-multiplying this expression by $\varphi_r(\hat{x}_k)$ and integration from $-\infty$ to ∞ yields the equation of motion of an equivalent SDOF system,

$$
\begin{aligned}
&\rho A_r \int_{-\infty}^{\infty} \varphi_r^2 \mathrm{d}\hat{x}_k \ddot{y}_{rk} + c_f \int_{-\infty}^{\infty} \varphi_r^2 \mathrm{d}\hat{x}_k \dot{y}_{rk} + E I_r \int_{-\infty}^{\infty} \varphi_r \varphi_{r,xxxx} \mathrm{d}\hat{x}_k y_{rk} \\
&+ k_f \int_{-\infty}^{\infty} \varphi_r^2 \mathrm{d}\hat{x}_k y_{rk} \\
&= \varphi_r F_k(t) \Pi(t, t_{Ak}, t_{Dk})
\end{aligned}
\tag{B.4}
$$

and further after inserting the shape function according to Eq. (B.1)

$$
\frac{3}{2\beta} \rho A_r \ddot{y}_{rk} + \frac{3}{2\beta} c_f \dot{y}_{rk} + \frac{2}{\beta} k_f y_{rk} = F_k(t) \Pi(t, t_{Ak}, t_{Dk})
\tag{B.5}
$$

since

$$
\int_0^{\infty} \varphi_r^2 \mathrm{d}\hat{x}_k = \frac{3}{4\beta} , \quad \int_0^{\infty} \varphi_r \varphi_{r,xxxx} \mathrm{d}\hat{x}_k = \beta^3
\tag{B.6}
$$

Appendix C. Coupling of substructures

Since $\dot{\Psi}_r^{(m)}(x = x_k(t)) = \frac{\mathrm{d}\Psi_r^{(m)}}{\mathrm{d}t} = \frac{\partial \Psi_r^{(m)}}{\partial x}\frac{\partial x_k}{\partial t} = v\Psi_{r,x}^{(m)}(x_k)$ and $\dot{I}_{\mathrm{irr}}(x = x_k(t)) = \frac{\mathrm{d}I_{irr}}{\mathrm{d}t} = \frac{\partial I_{irr}}{\partial x}\frac{\partial x_k}{\partial t} = vI_{\mathrm{irr},x}(x_k)$, as well as $\dot{\varphi}_r(\hat{x}_k(t) = 0) = 0$, the velocity and acceleration of the wheel at the axle position $x = x_k$ can be expressed as

$$
\begin{aligned}
\dot{u}_{ak}(x_k) =& \dot{w}_r(x_k, t) + \dot{I}_{\mathrm{irr}}(x_k) \approx \dot{y}_{rk} \\
&+ \sum_{m=1}^{N_b} \left(v\Psi_{r,x}^{(m)}(x_k)y_b^{(m)}(t) + \Psi_r^{(m)}(x_k)\dot{y}_b^{(m)}(t) \right) \\
&+ \sum_{m=1}^{N_b} \left(v\bar{\Psi}_{r,x}^{(m)}(x_k)\bar{y}_b^{(m)}(t) + \bar{\Psi}_r^{(m)}(x_k)\dot{\bar{y}}_b^{(m)}(t) \right) + vI_{\mathrm{irr},x}(x_k)
\end{aligned}
\tag{C.1}
$$

$$
\begin{aligned}
\ddot{u}_{ak}(x_k) =& \ddot{w}_r(x_k, t) + \ddot{I}_{\mathrm{irr}}(x_k) \\
\approx& \ddot{y}_{rk} + \sum_{m=1}^{N_b} \left(v^2 \Psi_{r,xx}^{(m)}(x_k)y_b^{(m)}(t) + 2v\Psi_{r,x}^{(m)}(x_k)\dot{y}_b^{(m)}(t) \right. \\
&\left. + \Psi_r^{(m)}(x_k)\ddot{y}_b^{(m)}(t) \right) \\
&+ \sum_{m=1}^{N_b} \left(v^2 \bar{\Psi}_{r,xx}^{(m)}(x_k)\bar{y}_b^{(m)}(t) + 2v\bar{\Psi}_{r,x}^{(m)}(x_k)\dot{\bar{y}}_b^{(m)}(t) + \bar{\Psi}_r^{(m)}(x_k)\ddot{\bar{y}}_b^{(m)}(t) \right) \\
&+ v^2 I_{\mathrm{irr},xx}(x_k)
\end{aligned}
\tag{C.2}
$$

The *corresponding assumption* yields the transformation matrix in Eq. (47) as

$$
\Gamma(t) = \begin{bmatrix} \mathbf{I}_b & \mathbf{0} & \mathbf{0} \\ \mathbf{0} & \mathbf{I}_r & \mathbf{0} \\ \mathbf{D}_b & \mathbf{D}_r & \mathbf{E}_c \end{bmatrix}
\tag{C.3}
$$

with the sub-matrices $\mathbf{I}_b$ and $\mathbf{I}_r$ denoting identity matrices of size $[2N_b \times 2N_b]$ and $[N_a \times N_a]$, respectively. The sub-matrices $\mathbf{D}_b$ and $\mathbf{D}_r$ result from the substitution of the DOFs of the axles by the displacement of the track at each axle position in Eq. (46) and can be expressed as

$$
\mathbf{D}_b(t) = \mathbf{E}_a \Pi(t) \Psi_r^{\mathrm{T}}(t)
$$
$$
\mathbf{D}_r(t) = \mathbf{E}_a \Pi(t) \mathbf{I}_r
\tag{C.4}
$$

with the previously defined matrix of window functions $\Pi(t)$ and the matrix of shape functions evaluated at the axle positions $\Psi_r(t)$. The sub-matrices $\mathbf{E}_c$ and $\mathbf{E}_a$ of Eqs. (C.3) and (C.4) read

$$
\mathbf{E}_c = \mathrm{diag} \left[\mathbf{J}_c^{(1)}, \mathbf{J}_c^{(2)}, \ldots, \mathbf{J}_c^{(N_c)} \right]
$$
$$
\mathbf{E}_a = \mathrm{diag} \left[\mathbf{J}_a^{(1)}, \mathbf{J}_a^{(2)}, \ldots, \mathbf{J}_a^{(N_c)} \right]
\tag{C.5}
$$

with

$$
\mathbf{J}_c^{(j)} = \begin{bmatrix} \mathbf{I}_c^{[6\times6]} \\ \mathbf{0}^{[4\times6]} \end{bmatrix} , \quad \mathbf{J}_a^{(j)} = \begin{bmatrix} \mathbf{0}^{[6\times4]} \\ \mathbf{I}_a^{[4\times4]} \end{bmatrix} , \quad j = 1, \ldots, N_c
\tag{C.6}
$$

The size of the identity matrix $\mathbf{I}_c$ is equal to the number of DOFs of the vehicle body and bogies of one vehicle of the train and the size of

the identity matrix $\mathbf{I}_a$ is equal to the number of axles involved in the coupling of one vehicle. Since in the present model of a conventional train each of the N_c vehicles is represented by a ten DOF system as depicted in Fig. 1, the matrices in Eq. (C.6) are equal for each vehicle. The vector $\mathbf{\Upsilon}(t)$ in Eqs. (47), (48), (49), containing the track irregularity profile function I_{irr} evaluated at each axle position, reads

$$\mathbf{\Upsilon}(t) = \begin{bmatrix} \mathbf{0}^{[(2N_b + N_a) \times 1]} \\ \mathbf{E}_a \mathbf{\Pi} \mathbf{I}_{irr} \end{bmatrix} \tag{C.7}$$

with the vector $\mathbf{I}_{irr}$,

$$\mathbf{I}_{irr}(t) = \begin{bmatrix} I_{irr}(x_1(t)), I_{irr}(x_2(t)), \dots, I_{irr}(x_{N_a}(t)) \end{bmatrix}^{\mathrm{T}} \tag{C.8}$$

References

[1] Willis R. Preliminary essay to the Appendix B: Experiment for determining the effects produced by causing weights to travel over bars with different velocities. Report of the commissions appointed to inquire into the application of iron to railway structures, W. Clowes and Sons; 1849.

[2] Stokes GG. Discussion of a differential equation relating to the breaking of railway bridges. Printed at the Pitt Press by John W. Parker; 1849, http://dx.doi.org/10.1017/CBO9780511702259.013.

[3] Frýba L. Dynamics of railway bridges. Thomas Telford Publishing; 1996, http://dx.doi.org/10.1680/dorb.34716.

[4] Frýba L. Vibration of solids and structures under moving loads. Springer Science & Business Media; 1999, http://dx.doi.org/10.1007/978-94-011-9685-7.

[5] Krenk S. Complex modes and frequencies in damped structural vibrations. J Sound Vib 2004;270(4–5):981–96. http://dx.doi.org/10.1016/S0022-460X(03)00768-5.

[6] Svedholm C, Zangeneh A, Pacoste C, François S, Karoumi R. Vibration of damped uniform beams with general end conditions under moving loads. Eng Struct 2016;126:40–52. http://dx.doi.org/10.1016/j.engstruct.2016.07.037.

[7] Di Lorenzo S, Di Paola M, Failla G, Pirrotta A. On the moving load problem in Euler–Bernoulli uniform beams with viscoelastic supports and joints. Acta Mech 2017;228(3):805–21. http://dx.doi.org/10.1007/s00707-016-1739-6.

[8] Foss KA. Coordinates which uncouple the equations of motion of damped linear dynamic systems. 1958;25:361–364.

[9] Yau J-D, Wu Y-S, Yang Y. Impact response of bridges with elastic bearings to moving loads. J Sound Vib 2001;248:9–30. http://dx.doi.org/10.1006/jsvi.2001.3688.

[10] Yang Y, Lin C, Yau J, Chang D. Mechanism of resonance and cancellation for train-induced vibrations on bridges with elastic bearings. J Sound Vib 2004;269(1):345–60. http://dx.doi.org/10.1016/S0022-460X(03)00123-8.

[11] Zangeneh A, Museros P, Pacoste C, Karoumi R. Free vibration of viscoelastically supported beam bridges under moving loads: Closed-form formula for maximum resonant response. Eng Struct 2021;244:112759. http://dx.doi.org/10.1016/j.engstruct.2021.112759.

[12] Hirzinger B, Adam C, Salcher P. Dynamic response of a non-classically damped beam with general boundary conditions subjected to a moving mass–spring–damper system. Int J Mech Sci 2020;185:105877. http://dx.doi.org/10.1016/j.ijmecsci.2020.105877.

[13] Wu Y-S, Yang YB, Yau J-D. Three-dimensional analysis of train-rail-bridge interaction problems. Veh Syst Dyn 2001;36:1–35. http://dx.doi.org/10.1076/vesd.36.1.1.3567.

[14] Salcher P, Adam C. Modeling of dynamic train–bridge interaction in high-speed railways. Acta Mech 2015;226(8):2473–95. http://dx.doi.org/10.1007/s00707-015-1314-6.

[15] Zhu Z, Gong W, Wang L, Li Q, Bai Y, Yu Z, Harik IE. An efficient multi-time-step method for train-track-bridge interaction. Comput Struct 2017;238:106270. http://dx.doi.org/10.1016/j.compstruc.2017.11.004.

[16] Galvín P, Domínguez J. High-speed train-induced ground motion and interaction with structures. J Sound Vib 2007;307(3):755–77. http://dx.doi.org/10.1016/j.jsv.2007.07.017.

[17] Ülker-Kaustell M, Karoumi R, Pacoste C. Simplified analysis of the dynamic soil–structure interaction of a portal frame railway bridge. Eng Struct 2010;32(11):3692–8. http://dx.doi.org/10.1016/j.engstruct.2010.08.013.

[18] Romero A, Solís M, Domínguez J, Galvín P. Soil–structure interaction in resonant railway bridges. Soil Dyn Earthq Eng 2013;47:108–16. http://dx.doi.org/10.1016/j.soildyn.2012.07.014.

[19] Svedholm C, Pacoste C, Karoumi R. In: Papadrakakis M, Papadopoulos V, Plevris V, editors. Modal properties of simply supported railway bridges due to soil–structure interaction. COMPDYN; 2015, p. 1709–19.

[20] Zangeneh A, Svedholm C, Andersson A, Pacoste C, Karoumi R. Identification of soil–structure interaction effect in a portal frame railway bridge through full-scale dynamic testing. Eng Struct 2018;159:299–309. http://dx.doi.org/10.1016/j.engstruct.2018.01.014.

[21] Bucinskas P, Andersen L. Dynamic response of vehicle–bridge–soil system using lumped-parameter models for structure–soil interaction. Comput Struct 2020;238:106270. http://dx.doi.org/10.1016/j.compstruc.2020.106270.

[22] Stoura CD, Dimitrakopoulos EG. A Modified Bridge System method to characterize and decouple vehicle–bridge interaction. Acta Mech 2020;1619–6937. http://dx.doi.org/10.1007/s00707-020-02699-3.

[23] Stoura CD, Dimitrakopoulos EG. Additional damping effect on bridges because of vehicle-bridge interaction. J Sound Vib 2020;476:115294. http://dx.doi.org/10.1016/j.jsv.2020.115294.

[24] Rocha J, Henriques AA, Calçada R. Probabilistic safety assessment of a short span high-speed railway bridge. Eng Struct 2014;71:99–111. http://dx.doi.org/10.1016/j.engstruct.2014.04.018.

[25] Hirzinger B, Adam C, Salcher P, Oberguggenberger M. On the optimal strategy of stochastic-based reliability assessment of railway bridges for high-speed trains. Meccanica 2019;54(9):1385–402. http://dx.doi.org/10.1007/s11012-019-00999-0.

[26] Cojocaru EC, Irschik H, Gattringer H. Dynamic response of an elastic bridge due to a moving elastic beam. Comput Struct 2004;82(11):931–43. http://dx.doi.org/10.1016/j.compstruc.2004.02.001.

[27] Johansson C, Nualláin NÁN, Pacoste C, Andersson A. A methodology for the preliminary assessment of existing railway bridges for high-speed traffic. Eng Struct 2014;58:25–35. http://dx.doi.org/10.1016/j.engstruct.2013.10.011.

[28] König P, Salcher P, Adam C, Hirzinger B. Dynamic analysis of railway bridges exposed to high-speed trains considering the vehicle–track–bridge–soil interaction. Acta Mech 2021;232(11):4583–608. http://dx.doi.org/10.1007/s00707-021-03079-1.

[29] Biondi B, Muscolino G, Sofi A. A substructure approach for the dynamic analysis of train–track–bridge system. Comput Struct 2005;83(28–30):2271–81. http://dx.doi.org/10.1016/j.compstruc.2005.03.036.

[30] Den Hartog JP. Advanced strength of materials. Dover books on engineering, New York: Dover Publications; 1987.

[31] Clough RW, Penzien J. Dynamics of structures. New York: McGraw-Hill; 1993.

[32] Das BM, Luo Z. Principles of soil dynamics. Cengage Learning; 2016.

[33] Wolf JP, Deeks A. Foundation vibration analysis: A strength of materials approach. Oxford: Butterworth-Heinemann; 2004.

[34] Popp K, Schiehlen WO, Kröger M, Panning L. Ground vehicle dynamics. Berlin: Springer; 2010.

[35] Knothe K. Rail vehicle dynamics. Cham, Switzerland: Springer; 2016.

[36] Biondi B, Muscolino G. Component-mode synthesis method for coupled continuous and FE discretized substructures. Eng Struct 2003;25(4):419–33. http://dx.doi.org/10.1016/S0141-0296(02)00183-9.

[37] Colinas-Armijo N, Di Paola M. Probabilistic analysis of the response of fractional viscoelastic railtrack under random train speed. Mecc Mater Strutt 2016;6:33–40.

[38] Dimitrovová Z. New semi-analytical solution for a uniformly moving mass on a beam on a two-parameter visco-elastic foundation. Int J Mech Sci 2017;127:142–62. http://dx.doi.org/10.1016/j.ijmecsci.2016.08.025.

[39] Bathe K. Finite element procedures. Boston, Mass: Bathe; 2006.

[40] Xia H, Zhang N, Guo WW. Analysis of resonance mechanism and conditions of train–bridge system. J Sound Vib 2006;297(3):810–22. http://dx.doi.org/10.1016/j.jsv.2006.04.022.

[41] Zhang N, Xia H, Guo W. Vehicle–bridge interaction analysis under high-speed trains. J Sound Vib 2008;309(3):407–25. http://dx.doi.org/10.1016/j.jsv.2007.07.064.

[42] Zhang N, Xia H, Guo WW, De Roeck G. A vehicle-bridge linear interaction model and its validation. Int J Struct Stab Dyn 2010;10(02):335–61. http://dx.doi.org/10.1142/S0219455410003464.

[43] Claus H, Schiehlen W. Modeling and simulation of railway bogie structural vibrations. Veh Syst Dyn 1998;29(sup1):538–52. http://dx.doi.org/10.1080/00423119808969585.

[44] Shinozuka M, Deodatis G. Simulation of stochastic processes by spectral representation. Appl Mech Rev 1991;44(4):191. http://dx.doi.org/10.1115/1.3119501.

[45] MATLAB (R2020a), Natick, Massachusetts, 2020.

[46] ABAQUS (2016), Providence, RI, United States, 2015.

[47] Rigueiro C, Rebelo C, Simões da Silva L. Influence of ballast models in the dynamic response of railway viaducts. J Sound Vib 2010;329(15):3030–40. http://dx.doi.org/10.1016/j.jsv.2010.02.002.

[48] Nguyen K, Goicolea JM, Galbadón F. Comparison of dynamic effects of high-speed traffic load using a simplified two-dimensional and full three-dimensional model. Proc Inst Mech Eng F 2012;228(2):128–42. http://dx.doi.org/10.1177/0954409712465710.

[49] Eurocode 1: Actions on structures - Part 2: Traffic loads on bridges.

[50] Yang YB, Yau JD, Wu YS. Vehicle–Bridge interaction dynamics, with applications to high-speed railways. World Scientific; 2004, http://dx.doi.org/10.1142/5541.

[51] Zarek JHB, Gibbs BM. The derivation of eigenvalues and mode shapes for the bending motion of a damped beam with general end conditions. J Sound Vib 1981;78(2):185–96. http://dx.doi.org/10.1016/S0022-460X(81)80032-6.

[52] Prater G, Singh R. Eigenproblem formulation, solution and interpretation for non-proportionally damped continuous beams. J Sound Vib 1990;143(1):125–42. http://dx.doi.org/10.1016/0022-460X(90)90572-H.

[53] Brandt A. Noise and vibration analysis: Signal analysis and experimental procedures/Anders brandt. Oxford: Wiley-Blackwell; 2011.

[54] Genta G. Vibration dynamics and control. Mechanical engineering series, New York: Springer; 2009.

[55] Hetényi M. Beams on elastic foundation: Theory with applications in the fields of civil and mechanical engineering. Mich: Scientific series, University of Michigan Ann Arbor, University of Michigan Press; 1946.